Development of a table-top neutral beam ion source for the study of insulation breakdown in DIII-D

Beckers, Jasper P.

Award date:
2018

Development of a Table-Top Neutral Beam Ion Source for the Study of Insulation Breakdown in DIII-D

Master Thesis - Jasper Beckers[1)]
B. Crowley[2)], J. T. Scoville[2)], R. J. E. Jaspers[1)], A. Sobota[1)]

[1)] *Eindhoven University of Technology, P.O. Box 513, 5600 MB Eindhoven, The Netherlands*
[2)] *DIII-D National Fusion Facility, General Atomics, P.O. Box 85608, San Diego, California, USA*

March 12, 2018

Neutral Beam Injection (NBI) is used for non-inductive heating, current drive, fueling, and diagnostics in most major present and future magnetic confinement fusion devices. The NBI system of the DIII-D device comprises of eight hot cathode ion sources of the CLPS design. Each of these can inject 2.5 MW of fast neutrals into the beamlines. The CLPS was developed in the eighties and has not been revised since. This has recently led to limitations in the operational capabilities of DIII-D, such as unreliability at higher injection power and failure during helium operation. This thesis presents the details and preliminary results of an experimental effort to develop a novel steady-state, table-top ion source with plasma parameters similar to the CLPS. The need for such a device arises from the desire to test and demonstrate methods to improve the performance and reliability of the NBI system. Numerical simulations were conducted to validate the confinement properties of the novel source design. The plasma was characterized on the aspects of discharge current modes, electron populations and spatial uniformity. A general agreement between behavior and theory was found. As an application, a study was performed on the electrical breakdown of gasket material during helium operation. The phenomenon was successfully replicated and it was found that certain design modifications can potentially mitigate the issue, increasing DIII-D capability. Further testing of these modifications on an actual CLPS source is planned at EAST, in China.

Contents

List of Figures

Glossary

		Ion source parameters
V	m^3	Chamber volume
S	m^2	Filament surface area
I_{arc}	A	Arc (discharge) current
V_{arc}	V	Arc (discharge) voltage
I_{fil}	A	Filament current
V_{fil}	V	Filament voltage
P_{fil}	W	Filament power
p_0	mTorr*	Background pressure
n_0	m^{-3}	Background neutral density
n_p	m^{-3}	Primary electron density
n_e	m^{-3}	Thermal electron density
n_i	m^{-3}	Ion density
f_p	-	Primary electron fraction
f_H	-	'Hot' thermal electron fraction
N_c	-	Number of cusps
T_0	K	Background neutral temperature
T_p	eV	Primary electron temperature
T_e	eV	Thermal electron temperature
T_i	eV	Ion temperature
T_{fil}	K	Filament temperature
B_{pm}	G†	Permanent magnet field strength
B_{cusp}	G†	Cusp field strength
ε_n	eV	Neutral injection energy
ε_p	eV	Primary electron energy
		Plasma fundamentals
λ_D	m	Debye length
ρ_c	m	Gyroradius
v_a	ms^{-1}	Acoustic (Bohm) velocity
$\ln\Lambda$	-	Coulomb logarithm

* 1 mTorr $\approx$ 0.133 Pa
† 1 G $= 10^{-4}$ T

1. Introduction

1.1 Motivation

The DIII-D device is a tokamak located in San Diego, California, at a facility operated by General Atomics and the US Department of Energy. Since its commissioning in 1986 it has been highly successful in conducting a wide variety of fusion research projects. For instance, it achieved the highest fusion reaction rate at the time [1]. These accomplishments were possible in part due to the powerful novel Neutral Beam Injection (NBI) technology, capable of injecting up to 20 MW of energetic particles into the fusion plasma. These NBI beams are used for non-inductive heating, current drive, fuelling, and diagnostics in both present and future devices.

DIII-D comprises of eight ion sources and accelerators that shoot energetic particles along a total of four individual beam lines. The ion sources are of the Common Long Pulse Source (CLPS) type, developed for American use in the 1980's. The chosen design was a filament-driven magnetic bucket ion source with acceleration grids. Over the past 30 years the CLPS devices have helped fusion research make remarkable progress, and have recently seen first operational use at the EAST facility in Hefei, China [2]. However, they have also faced difficulties [3, 4]. Especially steadily increasing performance requirements, which push the devices to their limits, and reliability issues are problematic for all facilities operating them. These reliability issues involve the formation of arc spots and performance deterioration, specifically during helium operation. CLPS has not been revised since its initial design by the Lawrence Berkeley Laboratory in the 1980's and no test stand exists in the US. Finding solutions to these bottleneck issues through development research would improve the capabilities of facilities such as DIII-D and EAST.

Therefore a table-top, scaled-down version of CLPS with similar plasma parameters is proposed. On this setup iterative design changes can be applied easily and rapidly, and reliability tests can be performed without requiring repairs that are expensive in terms of costs and time. The aim of this work is to design and develop this novel source, and apply it in a first research case.

An additional motivation for the construction of a smaller beam source is the capability of steady-state operation. Reliability issues are marked by a gradual deterioration of performance and the formation of destructive arc spots. These issues can take anywhere between tens of shots, especially during helium operation, to thousands of shots to affect operation of the source. This equals to days or entire experimental DIII-D campaigns. By incorporating the capacity of steady-state operation during the development of the new source it can be subjected to thousands of shots worth of deteriorating exposure in a matter of hours.

1.2 Research objectives

Based on the motivation and project definition the main research objective can be stated as follows:

> ***Develop and characterize a novel steady-state, table-top ion source for the study of insulation breakdown under helium operation.***

The main objective can be split into a number of logical research goals and questions. The structure of this thesis follows these sub-objectives, and they will be referenced throughout this work to provide context.

Prior to the discussion of any work, the introductory concepts relating to the background and motivation of this thesis will be presented. The corresponding research question is:

> *What is DIII-D and why is an improved NBI ion source reliability desired?*

Chapter 2 will discuss this. Subsequently follows an analysis of relevant theory in literature:

> *Identify and investigate important concepts in ion source literature relating to source plasma parameters and operational modes.*

This will be presented in chapter 3, which focuses on the aspect of plasma parameters, and chapter 4, which focuses on operational modes and durability. After this follows a treatment of the design and development of the novel source, which corresponds to the objective

> *Develop a scaled-down version of the CLPS ion source capable of steady-state operation and diagnostical flexibility.*

This will be detailed in chapter 5. This is directly followed by a numerical study of confinement properties, corresponding to the research sub-goal

> *Validate the confinement properties of the novel source using computational modelling.*

This will be presented in chapter 6. In light of initial use of the novel source a plasma characterization study follows. This relates to the objective of chapter 7:

> *Characterize the plasma parameters and operational modes of the new ion source and compare the results with theory.*

The last research goal corresponds to the latter part of the main research objective:

> *What CLPS improvements can be suggested based on replication and failure mechanism analysis of the insulation breakdown during helium operation?*

This study will be presented in chapter 8.

A general conclusion to the main research objective and a discussion of the future research outlook are found in the last chapter, 9.

2. Introductory concepts

- *What is DIII-D and why is an improved NBI ion source reliability desired?*

As the world is heading towards an era of clean energy production multiple technologies are being developed to satisfy the increasing demand. Some of these are already delivering power to the grid extensively, such as solar panels and wind turbines, while others are in the current state more experimental of nature. Prominent amongst these is nuclear fusion, a cleaner and safer alternative to nuclear fission. Instead of the exothermic splitting of heavy atoms, light particles are energetically fused together. This process releases a great deal of energy in what is known as a fusion reaction.

One of the most promising fusion reactions is that of Deuterium and Tritium:

$$^2\mathrm{D} +^3 \mathrm{T} \rightarrow {}^4\mathrm{He} + \mathrm{n} + 17.6 \text{ MeV}.$$

Because the gaseous reactants must be highly energetic they are in the so-called plasma state. This is necessary in order to have a sufficiently high reaction probability for net energy production. In the plasma state atoms become ionized and lose their electrons, resulting in a gas of charged particles. High susceptibility to electromagnetic fields is an important property of charged particles and is taken advantage of for confinement and acceleration.

2.1 Magnetic confinement fusion

Any self-heating fusion plasma is required to satisfy the Lawson criterion in order to reach ignition, which arises from the balance between energy production and loss [5]. This criterion states that the minimum product of the total ion density n and energy confinement time τ_E is given by

$$n\tau_E \geq \frac{12kT}{E_F \langle \sigma v \rangle},$$

where kT is the plasma temperature, E_F is the energy released in a fusion reaction, and $\langle \sigma v \rangle$ is the fusion reaction rate. In some schemes, such as inertial confinement fusion, a high density is favored over energy confinement time in order to satisfy this criterion. However, most resources are focused on the development of magnetic confinement fusion devices, which favour energy confinement.

The first of these magnetic confinement devices were of the tokamak type and developed in the 50's. The design quickly became regarded as the most promising candidate for net-energy producing fusion, and in the next decades the experimental tokamak devices increased in size and power.

2.1.1 DIII-D

The American DIII-D tokamak began operation in 1986 at a facility ran by General Atomics and the US Department of Energy in San Diego, California. It was based on the older Doublet III design and was designed to further investigate the shaping of plasmas in order to mitigate instabilities and increase performance. It has a highly elongated ($\kappa \leq 2$) D-shaped plasma chamber with a major radius $R = 1.66$ m and a minor radius of $a = 0.67$ m [1].

DIII-D has been successful in advancing the field of nuclear fusion and remains scientifically valuable. For instance, in the past it achieved both the largest plasma-to-magnetic pressure factor β and the highest fusion reaction rate at the time.

2.2 Neutral Beam Injection

- *Why is there a need for NBI in fusion and what is the CLPS?*

In order to heat the fusion plasma to the high temperatures needed auxiliary heating systems are required, which are an important aspect of every device. All large experiments use Neutral Beam Injection (NBI) along with other forms of heating such as Electron Cyclotron Heating (ECH) and Ion Cyclotron Heating (ICH). NBI systems are usually capable of injecting multiple megawatts of power into the plasma. In addition to non-inductive heating they are used for current drive and plasma fuelling. NBI is also at the basis of diagnostics such as Motional Stark Effect (MSE) and Charge Exchange Recombination Spectroscopy (CER).

The working principle of Neutral Beam Injection heating is the acceleration and successive neutralization of ions which enter the fusion plasma at high velocity and heat it collisionally. Neutralization of the ions is necessary in order to allow them to enter the magnetically confined plasma and not be repelled by the strong fields. Impacts with plasma ions and electrons transfer energy from the beam particles to the colder fusion plasma, as well as Coulomb collisions after charge exchange has taken place.

Some important considerations are the beam particle energy and slowing down time. The neutral energy should be large enough to sufficiently penetrate the plasma, but not cause beam shine-through. This can severely damage the reactor walls. Loss of beam power in undesirable locations is detrimental to the NBI efficiency. The efficiency will also decrease if the beam slowing-down time is larger than the particle confinement time. In that case beam particles are unable to transfer all energy to the fusion plasma and consequently heating power is lost.

A NBI system consists fundamentally out of three components: the ion source, the accelerating structure and the neutralizer. The focus of this work will be on the ion source. The purpose of the ion source is the generation of ions which subsequently enter the accelerating structure. In the lab environment and in various literature the ion source itself is often called the *arc chamber*. However, this terminology can lead to confusion as the plasma produced in the chamber is not a typical arc - in this case the thermionic emission that classifies arc discharges is externally induced, and thus the arc is *non-self-sustaining*. As will be described in section 2.2.3, the occurrence of actual self-sustained cross-electrode arcing events in the 'arc chamber' is highly undesirable. In the accelerator ions fall through a large potential difference and gain their directed kinetic energy. The energy gain is generally up to 120 keV for positive ion NBI systems and up to 1 MeV when negative ions are injected. Negative ions are required in high energy regimes because the neutralization efficiency of positives becomes very poor. In this thesis the focus will be on the generation of positive ions, however, since this is a defining factor for capabilities of devices such as DIII-D and EAST.

2.2.1 Common Long Pulse Source

DIII-D was the first device to pioneer Neutral Beam Injection (NBI) technology. In total DIII-D comprises eight positive ion sources of the Common Long Pulse Source (CLPS) design, injecting along four beam lines. Each source is capable of injecting 2.5 MW worth of fast neutrals adding up to a total heating power of 20 MW [6].

In the early 80's the United States consolidated their efforts into the development of a single neutral beam ion source. The main criteria were the performance requirements and space restrictions of the users at the time, which were TFTR at Princeton, MFTF-B at Lawrence Livermore National Laboratory, and DIII-D at General Atomics. The end result was the Common Long Pulse Source or CLPS [7], developed mainly at the Lawrence Berkeley Laboratory as an evolution of their Berkeley Multicusp Ion Source [8]. Recently the CLPS has also been commissioned for use in EAST, in China [9] (see figure 2.1).

The NBI systems at DIII-D are mostly operated at 80 kV, accelerating deuterium and hydrogen ions. Helium can also be used as injection gas, at reduced power. The injection duration is 3.5 s for 5 MW of power and 5.0 s for 4 MW. The energetic primary electrons that ionize the background gas originate from 32 tungsten filaments, pictured in figure 2.2.

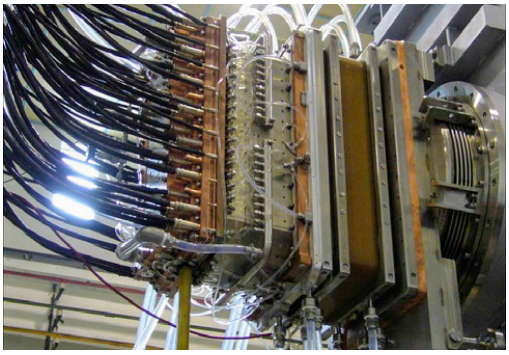

Figure 2.1: Photograph of a CLPS ion source at the EAST facility, from [9] with permission. The cables on the left deliver power to heat the filaments and create the potential difference between the cathode and anode. Lines inject gas into the chamber that is subsequently ionized by energetic electrons emitted from the hot filaments. The ions are incident on the grid structure that is located on the right hand side. Accelerated ions enter the neutralization chamber further to the right (not shown).

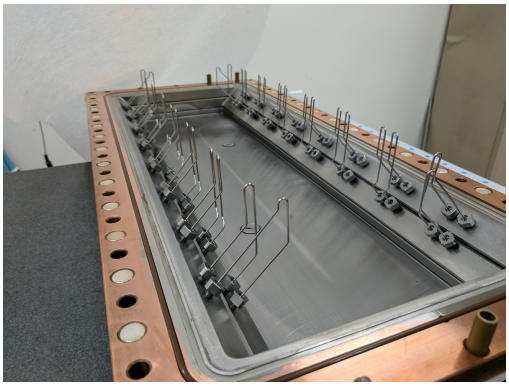

Figure 2.2: Photograph of an ion source under maintenance at DIII-D, showing exposed filaments. The source contains 32 tungsten filaments of varying shapes. Their typical length is 160 mm. The source itself is rectangular in order to provide a beam shape that fits through the narrow coil structure, with dimensions of approximately 26 by 65 cm.

2.2.2 Performance characterization

- *How is NBI performance characterized?*

Important measures of fusion-relevant neutral beam performance are the injected neutral energy ε_n and the beam current I_{beam}. In an ideal system the product of these yields the total injected power, $P_{inj} = \frac{I_{beam}}{e}\varepsilon_n$. Here the injection energy of the neutrals ε_n can be written as $\varepsilon_n = eV_{acc}$, which is a function of the acceleration potential that the ions from the source fall through. The beam current is equivalent to the ion flux incident on the grid surface area A_{grid}, taking into account the acceleration grid transparency T. This yields $I_{beam} = \frac{1}{2}en_i\sqrt{\frac{T_e}{m_i}}A_{grid}T$, where $\sqrt{\frac{T_e}{m_i}}$ is the ion acoustic velocity. Substitution of the previous equations gives

$$P_{inj} = \frac{1}{2}n_i\sqrt{\frac{T_e}{m_i}}A_{grid}TeV_{acc}. \tag{2.1}$$

This shows that the heating power can be increased through a higher acceleration voltage or a hotter and denser ion source plasma.

The operational performance of neutral beam ion sources is usually characterized by three factors: the arc chamber efficiency, the perveance and the beam divergence [10]. These will be discusses below.

Total efficiency

The total NBI efficiency is the ratio of output beam current to total input power P_{input}, ie.

$$\eta_t = \frac{I_{beam}}{P_{input}}. \tag{2.2}$$

This parameter has units of AW^{-1}. The total efficiency arises from the combined efficiencies of the ion source, accelerator, neutralizer, and particle energy transfer. The ion source efficiency is governed by eg. energetic electron utilization, particle confinement, and atomic mass fraction.

Perveance

Perveance is a measure of extracted beam current for a given acceleration voltage [11]:

$$\Pi_{beam} = \frac{I}{V^{\frac{3}{2}}}. \tag{2.3}$$

This equation arises from the space-charge limit. Perveance is measured with the unit $\mu\text{p} = \mu\text{perv} = 10^{-6}\text{AV}^{-\frac{3}{2}}$. Each Neutral Beam system is designed for some optimal perveance that corresponds with optimal acceleration grid optics.

Divergence

Divergence is the angular spread of the beam. Minimum divergence is met at the device-specific optimal perveance. Especially for turbulence suppression, where localized heating is desirable, low divergence is a necessity. This allows the beam to be targeted more accurately.

2.2.3 Reliability

- *What issues are observed regarding helium operation?*

The DIII-D fusion reactor can operate with a number of gases. Typically deuterium is used, with deuterium or hydrogen beams. Additionally, there exists a number of DIII-D research proposals that utilize helium discharges. Helium discharges are desirable for some diagnostical purposes, as well as to conduct research relevant for the ITER pre-nuclear phase. ITER will initially run helium and hydrogen discharges [12]. However, currently helium operation in DIII-D is undesirable due to issues that will be discussed next.

The CLPS ion sources, similar to most other devices, are subject to some level of deterioration due to operation. The severity of this deterioration depends on the way the device is being operated, such as duration, intensity, and background gas, which is most relevant to this work. Deterioration can decrease performance and may require repairs that are both cost and time expensive. An example of reliability problems caused by operation with helium is given during the Spring 2016 DIII-D experimental campaign.

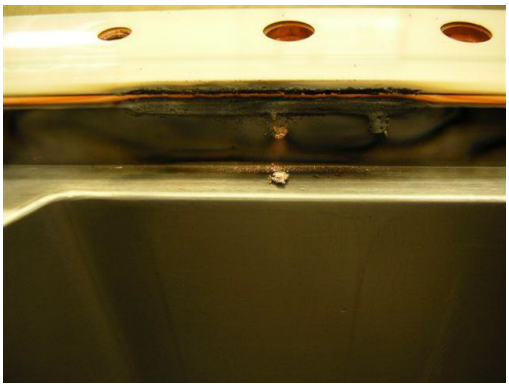

(a) Damage on the 150° left arc chamber plate and Mylar gasket.

(b) Damage on the 330° left arc chamber plate.

Figure 2.3: Photographs of ion source damage sustained after helium operation, taken from [13] with permission. Shown are the Mylar gaskets that are located in between the electrode sandwich. The black residue around the breakdown spots is carbonized insulation gasket. The oxidation patterns form during the breakdown process and are permanent if not removed by scrubbing.

The device was operated with helium NBI from April 18 through 22, 2016, but major issues prevented further continuation according to a report compiled afterward [13]. At the start of this period six neutral beams were converted for helium usage, but one source failed due to shorting of the chamber after only firing four shots. A second beam failed after a couple of days, resulting

in the decision to run the still-operational beams at a decreased performance for the remainder of the campaign. Helium operation led to deterioration of the insulation between the electrodes of the source. This reduced the plate-to-plate impedances from the magnitude of GΩs and MΩs to kΩs and in some cases internal short-circuits. This damage can be seen in the photographs of figure 2.3. These breakdowns occur across the electrode sandwich, indicated at the equivalent location in the new source in figure 2.5. The affected sources had to be disassembled, refurbished, and reassembled. The refurbishment process involves scrubbing the source interior and removing carbonized material, cleaning and filing the copper plates, and replacing the affected insulation gaskets. Sources have to be brought into the source lab, which involves disconnecting electrical and cooling lines and operating a heavy lift crane. In addition to the unavailability of the affected sources in the campaign following helium operation, it is estimated that the total repair costs equate to roughly $10.000.

Ion source discharges are generally more intense in helium versus hydrogen or deuterium. The underlying reason is the higher ionization potential which requires ion source discharges with higher voltage and pressure. Helium also has a smaller atomic radius, and thus permeates into materials, and a higher mass, leading to increased sputtering. One of the goals of this thesis is to build a table-top version of the CLPS source to further analyze the issues related to helium operation. Therefore the focus of the work presented here will be on source operation in helium.

Filament degradation is also common in hydrogen and deuterium plasmas, and more prominently in helium plasmas. The filaments lose mass during operation through sputtering and evaporation, which decreases their diameter and causes surface roughness, unevenness, or worse (see figure 2.4). This decreases their emissivity, requiring them to be ran at higher power and creating a vicious circle. At a certain point the filaments have to be replaced, requiring a similar procedure to what was described previously.

Figure 2.4: Detail of the degradation of four filaments after beam operation. The filaments are bent, and the surfaces pitted and rough. Various filaments are snapped in two.

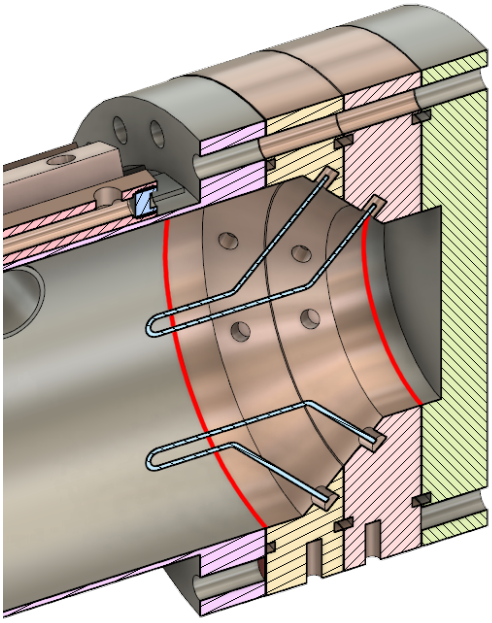

Figure 2.5: Detail of cathode-anode geometry in the novel ion source. The location of insulating gaskets where arc spotting occurs are indicated with red. A detailed description of the design and components will be presented in chapter 5.

3. Neutral Beam ion sources

• *Identify and investigate important concepts in ion source literature relating to source plasma parameters and operational modes.*

Before the development and initial experimental studies of the novel ion source the most important concepts in beam source physics will be treated, concerning plasma physics and operation. This measure of importance follows from primary principles and from certain criteria beam sources are ought to satisfy, which will first be discussed.

3.1 Beam ion source requirements

• *What are the criteria both the CLPS and miniature source should satisfy?*

Many types of ion sources exist, but few are capable of the output powers required of NBI systems in fusion. In addition, rigorous engineering and physics-related criteria are to be met. It is important to establish these requirements prior to proceeding, with the aim of identifying areas where the theoretical analysis and characterization process of the novel source should focus.

In essence NBI systems perform auxiliary tasks with the ultimate goal of increasing fusion power and providing diagnostical capabilities. In order to maximize their operational functionality and practicality several criteria should be met. Kunkel [14] defines 9 requirements for Neutral Beam ion sources, which will be referenced throughout the remainder of this work.

1. *Long-pulse operation*
   The source should be capable of operating steadily for the duration of a shot, typically a number of seconds. Parts of the source may require active cooling to dissipate heat.

2. *Uniform current-density profile*
   A non-uniform current-density profile incident on the accelerating structure has a negative effect on the grid optics, and thus divergence. This decreases the overall efficiency and also reduces the lifetime of the grids. In [6] Vella *et al.* describe an acceptable plasma uniformity of $< 15\%$ max/min.

3. *Low fluctuation level*
   Temporal fluctuations and noise prevent optimum acceleration grid optics and are also undesirable from an experimental point of view.

4. *Low ion temperature*
   The thermal energy of ions incident on the accelerator must be minimized to decrease random motion that negatively affects beam divergence. According to Kunkel T_i should therefore never exceed a few eV. This implies that the preferred method of increasing beam particle flux (see equation 2.1) is an increase in ion density, versus an increase in electron (and indirectly ion) temperature. Moreover, the injected particle flux scales more strongly with density than electron temperature.

5. *Ion species mix*
   The plasma species mixture in the source may contain diatomic or triatomic ions in addition to monatomic ions. These heavier ion species gain the same energy from the acceleration potential fall, but break up into multiple atoms during the subsequent neutralization process. This results in a fraction of neutrals having energies of $\frac{1}{2}\varepsilon_n$ or $\frac{1}{3}\varepsilon_n$, hence a high monatomic fraction in the source is favorable. In some literature [6] fractions of 80% and above are described as desirable.

6. *Low impurity level*
   Impurities present in the ion source plasma can accumulate and significantly degrade the fusion performance.

7. *Efficiency*
   This can be categorized into power and mass efficiency. Efficient ion sources tend to have an improved lifespan for a given operational schedule. Power efficiency is dominated by primary electron utilization and confinement.

8. *Reliability*
   For a Neutral Beam to be practical the ion source discharge should produce predictable, reliable plasmas.

9. *Ruggedness and durability*
   The ion source should not require high levels of maintenance. It should be able to run thousands of shots without component deterioration or failure.

3.2 DC hot cathode sources

- *What is the main operating principle of DC hot cathode beam sources?*

Numerous ionization processes are implemented in a wide variety of ion source designs. In DC sources such as CLPS electron bombardment ionization is utilized. Electrons are released into a chamber filled with background gas and subsequently accelerated. These energetic electrons bombard and ionize the gas. This principle is similar to sources used in electric space propulsion. However, the latter generally use hollow cathodes to emit electrons into the chamber. Neutral beam sources historically use heated filaments, although hollow cathode sources are in development for devices such as Lockheed Martin's Compact Fusion Reactor [15].

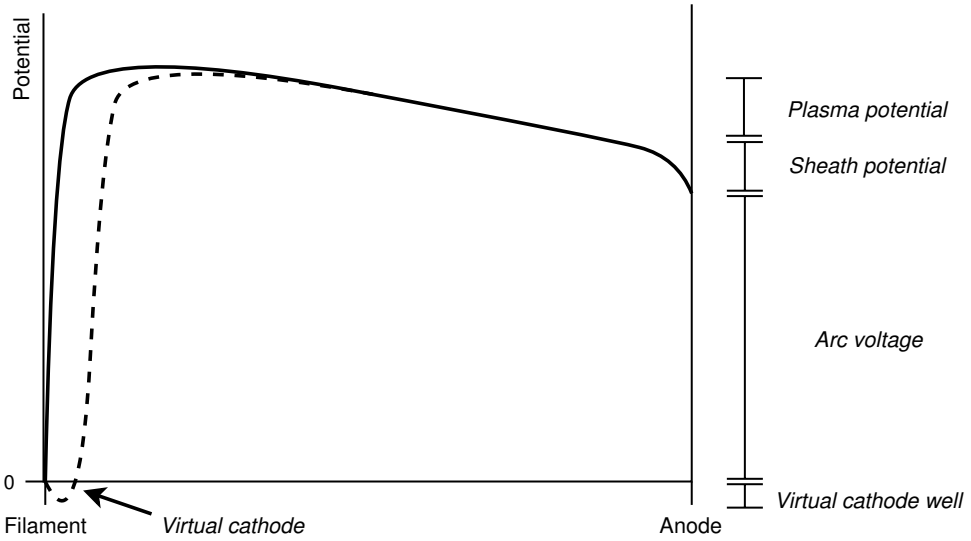

Figure 3.1: Schematic showing the potential distribution between the filament and anode inside the plasma chamber. Ratios are exaggerated. The dashed line indicates the situation where a significant negative space-charge is present around the filament. This phenomenon is called a virtual cathode (see section 4.1.2).

A DC voltage, V_{arc}, is applied between the heated cathodes and the anode walls of the chamber. Consequentially a potential distribution develops between the electrodes, which is perturbed by the presence of the plasma. Figure 3.1 shows a schematic of this distribution [16]. Electrons emitted from the filament that fall through this potential, also called primary electrons, gain the energy ε_p as they enter the plasma. This energy is defined as

$$\varepsilon_p = e\left(V_{arc} + V_p + \phi\right), \tag{3.1}$$

where V_p is the plasma potential and ϕ the sheath potential. For relatively large arc voltages the other terms are often discarded as in such cases eV_{arc} is the dominant term.

The emergence of a virtual cathode near the filament is also shown in figure 3.1. The underlying reason is the accumulation of negative space-charge in situations where the current emitted directly from the filament is significant compared to the current that is extracted from this region. This phenomenon will be discussed in more detail in section 4.1.2.

3.2.1 Thermionic emission

The emission of electrons from a heated filament is called thermionic emission. This phenomenon occurs because at elevated temperatures electrons have sufficient thermal energy to overcome the work function W of the material. For tungsten filaments $W = 4.52$ eV. The relation between the emission J_{em} and cathode temperature is given by the Richardson-Dushman equation [17]:

$$J_{em} = A_G T_{fil}^2 e^{-\frac{W}{kT_{fil}}}, \tag{3.2}$$

where $A_G = \lambda_R A_0$ is the product of the material specific value $\lambda_R \approx 0.5$ and the constant $A_0 = \frac{4\pi m_e k^2 e}{h^3}$, and T_{fil} is the local surface temperature.

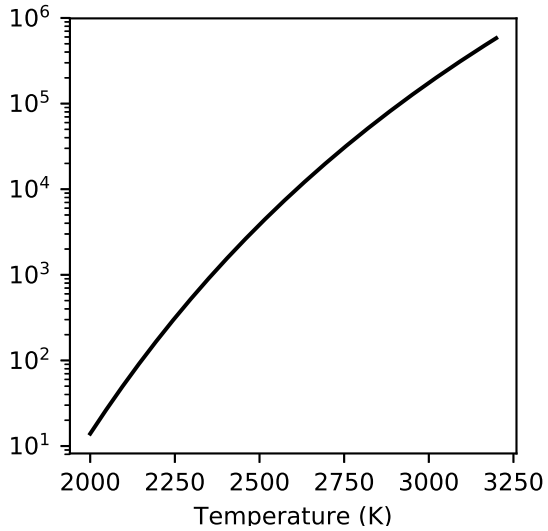

Figure 3.2: Thermionic emission density from a tungsten filament as function of temperature.

In figure 3.2 it is shown that equation 3.2 is a near quadratic function in the applicable temperature domain, for a tungsten filament. As a consequence the emission is sensitive to the local temperature. For instance, a temperature difference of $\pm 20°$ results in a relative emission difference of $\approx \pm 20$ %. These differences in local temperature arise when the filament temperature profile is non-uniform. This will be discussed in more detail in section 4.1.1.

In the DC-driven CLPS the cathode is biased negatively relative to the surrounding plasma. This gives rise to the Schottky effect, or field enhanced emission, which increases the thermionic emission current. The presence of an electric field reduces the work function [18]. This reduction, defined as $W' = W - \Delta W$, is given by

$$\Delta W = \sqrt{\frac{e^3 F}{4\pi\epsilon_0}}, \tag{3.3}$$

where F is the magnitude of the electric field at the surface. This cathode surface field is defined as the arc voltage V_{arc} over the high potential sheath thickness $s = \left(\frac{2\varepsilon_0 V_{arc}}{e n_s}\right)^{\frac{1}{2}}$:

$$F = \frac{V_{arc}}{s} = \sqrt{\frac{e n_s V_{arc}}{2\varepsilon_0}}, \tag{3.4}$$

where n_s is the electron sheath density. For typical discharge parameters the field is found to be $F \approx 270$ Vmm^{-1}, resulting in a work function reduction of $\Delta W = 0.02$ eV. This enhances the emission by factors from 1.12 to 1.08 for low to high surface temperatures, respectively. This shows that the Schottky effect is more significant when the emissivity is relatively low. It should be noted that in a certain operational mode the surface field strength will diminish or disappear entirely due to the presence of space-charge (see section 4.1.2). In that case the emission remains purely thermionic.

3.2.2 Ion production rate

- *Which populations govern the rate of ion production in the source?*

Primary electrons and the Maxwellian electron population (mostly the energetic tail) cause ionizing collisions with the background gas. The total ionization current is the sum of these two terms and can be written as

$$I_i = en_0 n_p \langle \sigma_i v_p \rangle V + en_0 n_e \langle \sigma_i v_e \rangle V, \tag{3.5}$$

where n_0 is the neutral density, n_p the density of primary electrons, n_e the thermal electron density, V the total plasma volume and σ_i the electron bombardment ionization cross section. The ionization rate is the product of the cross section [19] and the bombardment velocity at a specific energy. In the case of a fully thermalized electron population a Maxwellian energy distribution applies. The mean ionization rate of such a population is then calculated as follows:

$$\langle \sigma_i v_e \rangle = \int_0^\infty \sigma_i^E v_e(E)\, 2\sqrt{\frac{E}{T_e}} \left(\frac{1}{T_e}\right)^{\frac{3}{2}} \exp\left(-\frac{E}{T_e}\right) \mathrm{d}E, \tag{3.6}$$

where σ_i^E is the ionization cross section at energy E and T_e is the mean temperature of the thermalized electrons. This expectation value is simply the first moment of the Maxwellian probability density. The monoenergetic reaction rate is defined similarly, but with the energy distribution function being a δ-peak at ε_p. The monoenergetic and Maxwellian ionization rates are shown in figure 3.3.

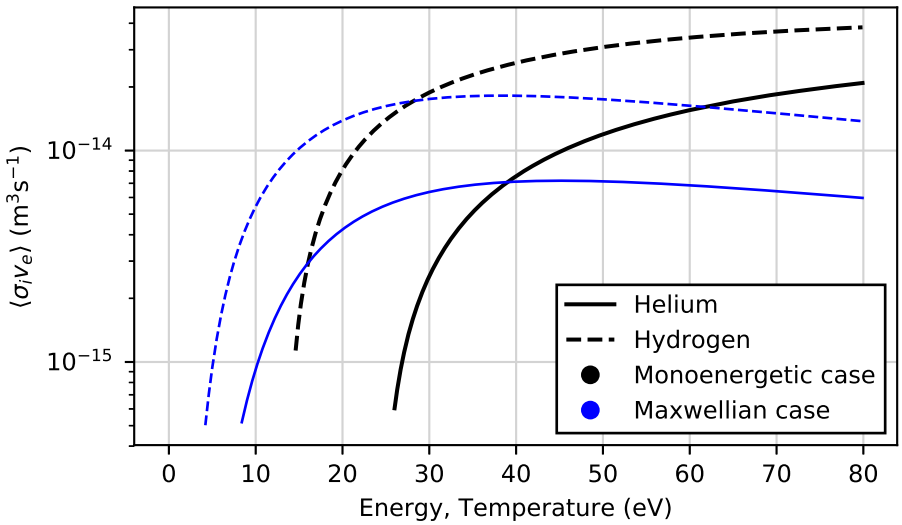

Figure 3.3: Helium and hydrogen electron-impact ionization reaction rate from [19], for monoenergetic and Maxwellian populations. It shows that the expected ionization reaction rate is orders of magnitude smaller for low temperature Maxwellian distributions compared to that of energetic primary electrons. Hydrogen has a lower ionization threshold than helium, thus the rates are higher at lower energy.

For a helium background gas the ionization threshold energy is 24.6 eV. The reaction rate expectation value of any Maxwellian distribution is non-zero due to the high energy tail. However, it is found to be orders of magnitude smaller compared to that of monoenergetic primary energies at arc energy for temperatures lower than a few electronvolt. This low thermal electron temperature is the case if the Kunkel ion source criteria are met (see Requirement 4, section 3.1). One additional consideration is that the thermal electron population density is generally greater than the primary electron density. However, this ratio $\frac{n_e}{n_p} = f_p^{-1}$ is expected to be in the range of 3 orders of magnitude (see section 3.4.2). This remains smaller compared to the difference in ionization reaction rate for low thermal temperatures ($T_e \leq 2$ eV). Thus, for simplicity, the thermal electron term in equation 3.5 can be discarded. Under the assumption that the primary electrons can be considered truly monoenergetic equation 3.5 reduces to

$$I_i = en_0 n_p \sigma_i^p v_p V, \tag{3.7}$$

where σ_i^p is the cross section at the primary electron energy (ie. arc voltage).

Atomic hydrogen has a lower electron bombardment ionization threshold energy at 13.6 eV, compared to helium. Consequently the reaction rates are higher and an overall lower electron temperature and/or density suffices to provide the same ionization current. The same holds for the di- and triatomic hydrogen species, of which the number fraction is assumed to be low (Requirement 5). The fundamental need for a more intense helium discharge compared to other background gases is the origin of several issues involving helium operation.

3.2.3 Primary electron timescales

- *How do primary electron losses impact efficiency and can this be quantified?*

An important measure of a DC hot cathode ion source performance is the primary electron utilization efficiency (see Requirement 7, section 3.1). This efficiency decreases if the primary electron ionization timescale becomes larger than the other loss timescales, thermalization and ballistic. In such a situation a significant fraction of the primary electrons in the source does not contribute to the ionization rate.

Primary electrons are lost either through inelastic ionization processes, through direct loss to the anode or through thermalizing Coulomb collisions with the Maxwellian electron population [20]. Thus, the effective primary electron lifetime τ_p can be written as the reciprocal sum of these timescales:

$$\frac{1}{\tau_p} = \frac{1}{\tau_i} + \frac{1}{\tau_b} + \frac{1}{\tau_{rel}}, \tag{3.8}$$

where τ_i is the mean ionization time, τ_b is the ballistic loss term and τ_{rel} is the relaxation time.

Under the assumption of monoenergetic primaries τ_i can be evaluated in a straightforward manner:

$$\tau_i = \frac{1}{n_0 \sigma_i^p v_p}, \tag{3.9}$$

which arises from equation 3.7. A higher primary energy and neutral density result in a shorter mean ionization time.

Direct loss to the anode is called ballistic loss. Curvature B-drift arising from the confining magnetic fields reduces the loss area for primary electrons to A_{pa}. In these cusps magnetic field lines are perpendicular on the surface. Electrons not directly incident on a cusp are magnetically reflected. This will be discussed in greater detail in section 3.3. The effect of diffusion is insignificant here as the electron density is relatively low and uniform. An equivalency can be defined between the 'effective' volumetric ballistic loss and the anode wall loss, ie. $n_e v_p A_{pa} \equiv \frac{n_e V}{\tau_b}$, where τ_b is the loss timescale and V the plasma volume. From this definition follows

$$\tau_b = \frac{V}{v_p A_{pa}}. \tag{3.10}$$

Equation 3.10 agrees with the expectation that the mean ballistic loss timescale increases with volume and decreases with loss area and primary electron energy.

The primary electrons are fast compared to the thermalized population; the squared velocity ratio $x = \left(\frac{v_p}{v_e}\right)^2 \approx \frac{T_p}{T_e}$ is typically in the range of 20 to 80, therefore $x \gg 1$. The volumetric slowing-down rate $\nu_s^{p,e}$ that is associated with the interaction of a primary electron with energy ε_p in a field of Maxwellian electrons with density n_e is given by [21]

$$\nu_s^{p,e} = 7.7 \cdot 10^{-12} \frac{\ln\Lambda}{\varepsilon_p^{\frac{3}{2}}}. \tag{3.11}$$

Here the Coulomb logarithm $\ln\Lambda$ is defined as $\ln\Lambda = 23 - \frac{1}{2}\ln\left(\frac{10^{-6} n_e}{T_e^3}\right) \approx 11$. The relaxation timescale that arises from equation 3.11 is then defined as the inverse of this rate, ie. $\tau_{rel} = \frac{1}{\nu_s^{p,e} n_e}$.

Due to the mass difference the electron-ion energy transfer is poor compared to that of electron-electron collisions. Hence electrons thermalize into a Maxwellian population, but do not thermalize with ions. As a consequence large discrepancies between electron and ion temperature ($\frac{T_e}{T_i} \geq 10$) are expected in the source [16].

Table 3.1: Typical discharge parameters during CLPS operation.

Parameter	Assumed value
n_i	10^{17} m^{-3}
T_e	2 eV
n_0	$6 \cdot 10^{20}$ m^{-3}
ε_p	80 eV

3.2.4 Timescale evaluation

For a satisfactory primary electron utilization efficiency the following condition should hold:

$$\tau_{rel}, \tau_b \gg \tau_i. \tag{3.12}$$

For typical ion source parameters, given in table 3.1, these timescales are evaluated. The results are shown in table 3.2.

Table 3.2: Primary electron timescale magnitudes.

Timescale	Magnitude
$\tau_i \approx \tau_p$	10^{-7} s
τ_b	10^{-4} s
τ_{rel}	10^{-4} s

It is found that generally the primary electron utilization efficiency condition (see 3.12) holds and that from equation 3.8 follows that $\tau_p \approx \tau_i$. The effective primary electron lifetime is dominated by the mean ionization timescale τ_i.

3.3 Magnetic multipole confinement

- *Why is there a need for confinement and how does confinement affect loss currents?*

The ionization mean free path λ_i can be estimated for typical discharge parameters. In the case of 80 eV primary electrons and a neutral helium density of $6 \cdot 10^{20}$ m^{-3} (see the typical discharge parameters, table 3.1) λ_i is found to be

$$\lambda_i = \tau_i^p v_p \approx 47 \text{ cm}. \tag{3.13}$$

This mean free path is greater than the source geometry and shows the need for confinement. Confinement increases the path length of primary electrons inside the chamber, and thus prevents premature wall loss.

Empirical studies have resulted in the development of several magnetic field designs, one of which is the magnetic multipole. This configuration was first proposed by Moore in 1969 [22] for use in ion thrusters. Permanent magnets of alternating polarity form a checkerboard pattern along the plasma boundaries. These create strong field cusps near the walls and cancel out in the center, where the field strength becomes negligible. Primary electrons are released into the plasma from the filament cathodes in a weakly diverging magnetic field. Consequently they are reflected off the relatively strong surface fields until they lose energy in collisions or are lost in a cusp.

In CLPS permanent magnets with a strength of $B_{pm} \approx 3000$ G (= 0.3 T) are embedded in the walls. The effective magnetization of a particle species can be examined by comparing the gyration radius with the chamber dimensions. In a magnetic field the electron gyration radius or Lamor radius ρ_c is given by

$$\rho_c = \frac{mv_\perp}{eB}, \tag{3.14}$$

where B is the local magnetic field strength, $v_\perp$ is the perpendicular velocity of the particle and m is the particle mass. Near the edge of the plasma the field strength increases towards B_{cusp} due to the magnetic cusp structure. Per definition $B_{cusp} < B_{pm}$ due to the finite wall thickness separating the plasma and the permanent magnet.

Magnetization of particles reduces their loss area to that of the magnetic cusps, where field lines are perpendicular to the anode. The anode loss area of primary electrons in circular cusps is given by

$$A_{pa} = \pi \rho_{cp}^2 N_c, \tag{3.15}$$

where N_c is the number of multipole cusps. For the miniature ion source this number is $7 \cdot 16 = 112$. Similarly the Maxwellian electrons are lost in the cusps, but their motion is affected by the plasma ions. A hybrid loss area A_{ea} is defined [20]:

$$A_{ea} = \pi \rho_{ce} \rho_{ci} N_c. \tag{3.16}$$

By substituting equation 3.14 it is found that the loss areas are proportional to $\varepsilon B_{cusp}^{-2}$, where ε is the respective species energy.

3.3.1 Losses

The thermal electron loss to the anode cusps is defined by the random electron flux times the Boltzmann factor:

$$I_{ea} = \frac{1}{4} \left(\frac{8kT_e}{\pi m_e} \right)^{\frac{1}{2}} n_e A_{ea} e^{-\frac{e\phi}{kT_e}}, \tag{3.17}$$

where A_{ea} is the total Maxwellian electron cusp loss area as defined by equation 3.16. ϕ is the sheath potential, which develops due to charged particle loss to the anode. Similarly, the ion loss currents to the cathode, I_{ic}, and anode, I_{ia}, are the products of the ion density n_i, the acoustic velocity v_a and the respective loss areas:

$$I_{ia} = \frac{1}{2} n_i e v_a A_{ia}, \tag{3.18a}$$

$$I_{ic} = \frac{1}{2} n_i e v_a A_c. \tag{3.18b}$$

Here the v_a is given by the Bohm velocity $\sqrt{\frac{kT_e}{m_i}}$ [23]. These currents are therefore also called Bohm currents. The ion cathode loss current I_{ic} is incident on the total cathode surface area A_c, which is equal to or larger than the filament surface area S depending on the internal geometry. The filament is not necessarily the only cathode surface exposed to the plasma, but can be considered the only emitting one.

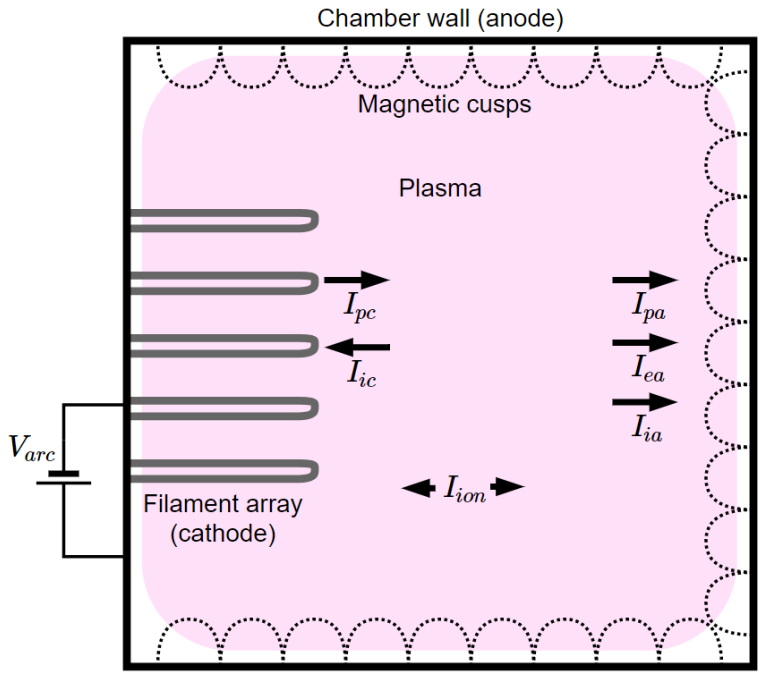

Figure 3.4: Components and species flows in an ideal hot cathode ion source. The primary current entering the plasma from the cathode is given by I_{pc}. Similarly, I_{pa} is the primary current leaving the plasma at the anode. The remaining primary electrons are involved in ionization, which is given by the current I_{ion}. Ion leave the plasma at both the cathode and anode, given by the current I_{ic} and I_{ia}, respectively. Finally thermal electrons, mainly produced as ionization products, are lost at the anode. This current is given by I_{ea}. All currents are defined as positive.

3.4 Ideal source

- *What can be learned from a simple ideal source model?*

A simplified, ideal ion source model can be used to obtain understanding of the underlying physics regarding parameters relevant to the source requirements and operation [16]. Consider an ion source as seen in figure 3.4. Normally the plasma volume is not well defined, but here it is assumed that the plasma is confined to a volume V with a uniform density profile. An arbitrary array of filaments releases a current of primary electrons into the chamber. It is assumed that every primary is involved with an ionizing reaction, and that quasi-neutrality holds inside the plasma.

3.4.1 Charge flux balance

Sheaths are considered collisionless. Under the assumption of ambipolar ion and electron loss to the anode, equating the thermal electron and ion losses (equations 3.17 and 3.18a, respectively) yields an expression for the floating sheath potential ϕ:

$$\phi = \frac{kT_e}{e} \ln\left(\sqrt{\frac{2m_i}{\pi m_e}} \frac{A_{ea}}{A_{ia}}\right). \tag{3.19}$$

Here it is also assumed that the primary loss current is negligible compared to that of the Maxwellian electron population. As expected this equation depends strongly on the electron temperature, and to a lesser extend on the ratio of the electron and ion loss areas. With typical operational parameters (see table 3.1) this model results in $\phi = -5$ V.

3.4.2 Particle balance

In the ideal ion source the ion production term is equal to the ion wall loss. This is under the assumption of negligible recombination due to relatively low pressures. Equating equations 3.7 and the sum of 3.18a and 3.18b provides an expression for the primary electron density fraction $f_p = \frac{n_p}{n_i}$:

$$f_p = \frac{e}{n_0 \langle \sigma_i^p v_p \rangle} \sqrt{\frac{T_e}{m_i}} \frac{A_{ia} + A_c}{V}. \tag{3.20}$$

Consequently a higher electron temperature results in a larger primary fraction necessary to sustain ion particle balance, as the ion wall loss term is increased. Equation 3.20 also highlights the proportionality between primary density and background pressure. A decrease in background pressure leads to an increase in primary electron density to compensate for the diminishing ionization current, and as a result of decreased primary electron loss. The fraction can be evaluated with typical parameters and is expected to be of a magnitude of 10^{-3} or lower.

The primary production, given by the thermionic emission term, must be equal to the primary loss through ionization assuming ionization is the dominant primary electron loss term. This is the case if the background pressure is large enough to ensure each primary electron undergoes an ionization process. In turn ion loss must be equal to the ionization production term. Thus a balance between primary production and ion loss arises, from which an expression for the ion density can be derived:

$$n_i = \frac{2 I_{pc}}{e} \sqrt{\frac{m_i}{T_e}} \frac{S}{A_{ia} + A_c}. \tag{3.21}$$

Thus the ion density is proportional to the ratio of filament and anode areas, intuitively corresponding to the ratio of primary electron production and loss.

3.4.3 Limitations

- *What are the limitations and assumptions used?*

Due to localized emission DC hot cathode ion sources have a spatially varying primary density, resulting in a non-uniform plasma. Additionally the assumption of a monoenergetic primary electron distribution fails as usually a spread in energies is measured [24, 25]. This changes the ionization and relaxation rates slightly.

Furthermore it was assumed that (monoenergetic) primary electrons dominate the ionization rate due to the increased reaction cross section. The inclusion of ionization by Maxwellian electrons increases the overall ionization rate and consequently increases the expected ion density for a given electron temperature and loss area (see equation 3.21).

4. Source operation

4.1 Operational modes

- *What operational modes exist?*

During ion source operation two distinct modes can be identified regarding the generation of primary electrons in the source, which directly corresponds to the ionization intensity. This significantly affects the working and performance of both the CLPS and miniature beam source. The modes are characterized by differences in sheath physics at the cathode. If the filament power is relatively low all emitted primary electrons find their way into the plasma. This is called the *emission limited* mode. In the limit of high filament power the current density entering the plasma will be *space-charge limited*.

4.1.1 Emission limited

In the emission limited mode there exists no limiting current density due to space charge. Electrons emitted from the cathode experience no repulsing force and flow freely into the plasma; every electron is accelerated towards the anode. In the limit of zero space-charge the current entering the plasma is exactly equal to the thermionic emission of the filament, and thus purely a function of the filament temperature.

The thermionic emission of primary electrons is given by equations 3.2 and 3.3. Due to the strong temperature dependence, the emission limited mode is also sometimes called the temperature limited mode. The temperature arises from the balance of heating and cooling terms. The arc-like plasma created in the source is non-self-sustaining, which implies that the cathode is mainly externally heated. The primary mechanism is resistive heating and given by the equation

$$P_{res} = V_{fil} I_{fil}. \tag{4.1}$$

Here V_{fil} and I_{fil} are the filament voltage and current, respectively. Usually the filament power supply is operated in current-limited mode, which implies that the heating power is proportional to the squared current. Additionally, during plasma operation, the cathode heats through ionic bombardment:

$$P_{ion} = \frac{1}{2} \varepsilon_i n_i v_a S, \tag{4.2}$$

where $\varepsilon_i = eV_{arc}$ is the ion impact energy, v_a is the ion acoustic velocity and S is the filament area. Equation 4.2 arises from the Bohm current density in the sheath, carrying the energy gained in the discharge potential to the surface. Radiative cooling is a cause of heat loss and is given by the Stefan-Boltzmann law,

$$P_{rad} = \sigma T_{fil}^4 S, \tag{4.3}$$

where σ is the Stefan–Boltzmann constant and T_{fil} is the local filament surface temperature. Electrons emitted thermionically also carry energy, cooling the filament [26]. This electron-emissive cooling power is given by

$$P_{em} = \frac{S I_{em}}{e} \left(\frac{3}{2} k T_{fil} + W - \Delta W \right), \tag{4.4}$$

where W and ΔW are the material work function and the Schottky effect given in equation 3.3, respectively. The consequences of these terms will be described in more detail in section 4.1.4.

4.1.2 Space-charge limited

If the source cathode is highly emissive a negative space-charge will build up around it. This is especially significant directly adjacent to the filament, where the particles have not yet been accelerated by the sheath and have low initial velocities. The negative space-charge imposes a limit on the current released from the cathode; a large fraction of the emitted electrons will be repelled back by the negatively charged electron cloud. This effect can be seen in figure 3.1. The position at which the potential is zero moves away from the cathode creating a so-called virtual cathode or double sheath. This effect was first described by Langmuir in 1929 [27, page 971]:

> *As the cathode temperature is raised the electron current density I_e increases and is equal to the electron emission from the cathode until... ...the current becomes limited by space charge and a further increase in electron current cannot occur. The cathode is then covered by a double layer or double sheath...*

Child's space-charge law states that the limiting current density between two electrodes is a function of the applied potential to the power three-halves and inversely with the inter-electrode distance squared [28, 29]. Using a simple one-dimensional model this can be derived as follows. Consider two infinitely large parallel plates over which a potential V is applied. Between these plates a certain electron current flows freely (ie. collisionless) with current density J. Charge conservation states that in the absence of charge sources or sinks the current density will be constant regardless of the position x between the plates:

$$J(x) = en_e(x)v(x) = J_0, \tag{4.5}$$

where the electron flux is the product of the density and velocity at each position. The current arises from the potential difference ϕ between the charged plates. Following the law of energy conservation electron velocity is dictated by the local potential $\phi(x)$:

$$e\phi(x) = \frac{1}{2}m_e v(x)^2. \tag{4.6}$$

The potential distribution is given by Poisson's equation for electrostatics. Combined with 4.5 and 4.6 this results in the differential equation

$$\Delta^2\phi = \frac{J}{\epsilon_0 v} = \frac{J}{\epsilon_0}\left(\frac{2e\phi}{m_e}\right)^{-\frac{1}{2}}, \tag{4.7}$$

where ε_0 is the vacuum permittivity. Assuming the boundary conditions that ϕ is zero at $x = 0$ and $\phi(d) = V$, equation 4.7 can be solved for a solution for the limiting current density. This solution is given by

$$J_{Child} = \frac{4\epsilon_0}{9}\sqrt{\frac{2e}{m_e}}\frac{V^{\frac{3}{2}}}{d^2}, \tag{4.8}$$

where d is the inter-electrode distance.

Double sheath modification

A modification of equation 4.8 can be made for the case where the limiting current flow is between two plasmas of different potentials, such as is the case in the double sheath situation [30]. As was previously described, this situation arises when a space-charge layer, or virtual sheath, is formed around the thermionic filament. The depth V_{vc} of this potential well (see figure 3.1) is proportional to the initial energy of the electrons that are emitted from the filament ε_{em}, thus a function of the filament temperature. $V_{vc} \approx -\frac{\varepsilon_{em}}{e} = -\frac{3}{2}\frac{kT_{fil}}{e}$, which is of the order of -0.3 V.

Substituting the electrode potential difference by the arc voltage $V \to V_{arc}$ and the inter-electrode distance by the expression for a high potential sheath thickness $d \to \left(\frac{2\epsilon_0 V_{arc}}{en_e}\right)^{\frac{1}{2}}$ in equation 4.8 yields the expression

$$J_{lim} = \frac{2}{9}e\sqrt{\frac{2eV_{arc}}{m_e}}n_e. \tag{4.9}$$

Thus it is found that the space-charge limited current scales with $J_{lim} \propto n_e\sqrt{V_{arc}}$. One consideration to be made is that the presence of a virtual cathode enhances the sheath thickness, an effect that is not taken into account in equation 4.9. Since equation 4.8 scales strongly with inter-electrode distance this can significantly decrease the limiting current density.

4.1.3 Mode transition

- *What governs the transition between these modes?*

The actual current of energetic primary electrons entering the plasma from the (virtual) cathode I_{pc} cannot exceed the thermionic current given by the Richardson-Dushman equation 3.2 and cannot exceed the current limit imposed by space-charge. Therefore I_{pc} is given by the smallest of these currents. In proper notation:

$$I_{pc} = S \cdot \min\left(J_{R-D}, J_{SCL}\right). \tag{4.10}$$

Hence, which mode is active can be controlled by adjusting either the filament temperature or the discharge voltage. Increasing the filament power brings the source into the space-charge limited mode, whilst inversely increasing the discharge voltage brings the source into the emission limited mode.

4.1.4 Operational stability

- *How do the modes affect stability?*

Especially in the emission or temperature limited mode the discharge parameters are very susceptible to the filament temperature profile as was shown in section 3.2.1, describing thermionic emission. During the ion source discharge heating of the filament through ion bombardment occurs, see equation 4.2. Additionally, electrons originating from the neutralizer can backstream through the acceleration grids into the arc chamber during beam operation, which also bombard the filaments and cause an increase in temperature [31].

The CLPS is usually operated in space-charge limited mode as the relatively high sensitivity to local temperature fluctuations of the filament in emission-limited mode is undesirable during operation (see section 3.1, Requirement 3). This requires the filaments to be ran at high power, reducing their lifetime.

4.2 Filament deterioration

- *What effect does helium operation have on filament deterioration?*

As described in section 2.2.3 deterioration reduces the filament lifespan and overall source reliability, especially during helium operation. During operation the filaments are subject to ion bombardment and thermal evaporation. Both mechanisms cause a loss of material, which has a high probability of becoming ionized and being deposited in the cusps. Moreover, during the pre-plasma phase of a shot the material lost from evaporation can be deposited on any inner chamber surface or insulation gasket. Thus, filament deterioration imposes a limit on the operational lifespan of the source. The effects of material loss are cumulative, ie. the condition of a filament is a consequence of all previous shots.

It should be noted that whilst bombardment sputtering is determined by the operational background gas, evaporation is not. This is important in the face of analyzing source deterioration and failure during helium operation.

4.2.1 Sputtering

Ions bombarding the filament gain the same energy primary electrons do falling through the cathode potential, given by equation 3.1. The sputter yield Y is the mean number of released particles of the target material per incoming energetic ion. Y is a function of the incident energy, energy transfer efficiency and incoming angle. Each ion-target pair has a particular

energy threshold below which no sputtering occurs. Assuming a normal angle of incidence this threshold energy can be readily calculated. The energy transfer efficiency is given by

$$\gamma = \frac{4Mm_i}{(M+m_i)^2}, \tag{4.11}$$

where M is the atomic mass of the target material and m_i is the mass of the incoming ion. The threshold energy is then

$$E_{threshold} = \frac{E_B}{\gamma(1-\gamma)}, \tag{4.12}$$

where E_B is the target binding energy. From equation 4.12 follows a threshold energy of 104.8 eV for helium ions incident on tungsten. This threshold energy is reflected in the sputter yields for specific energies from theory by Yamamura and Tawara [32], see figure 4.1.

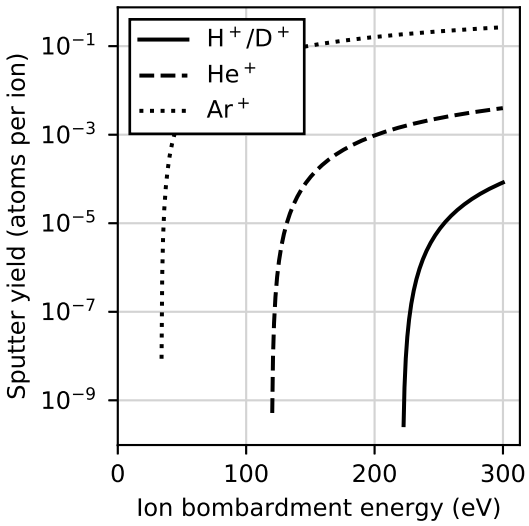

Figure 4.1: Ion bombardment sputter yields of tungsten [32]. The ions are assumed to have an incidence normal to the surface. The sputter threshold agrees with equation 4.12.

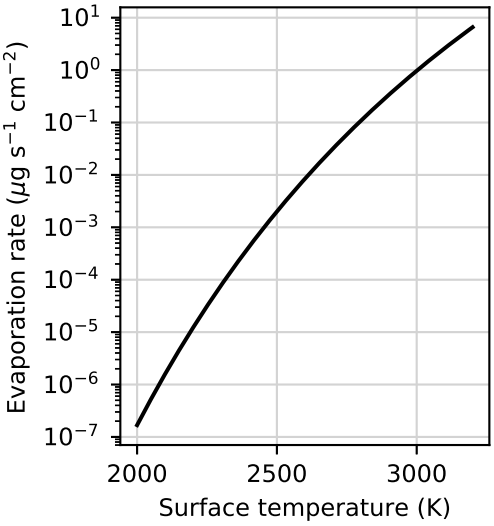

Figure 4.2: Evaporation rate of tungsten filaments, from [33]. The rate is given in μg per second per cm^2.

Figure 4.1 shows that no hydrogen or deuterium sputtering can occur in the source, and only helium sputtering during operation at unusually high primary electron energies. However, during helium operation a processed called 'argon frosting' is used to prepare the gas lines for the pumping of helium. The figure shows that, since argon is an atom of larger mass, the sputter threshold is far lower and the overall yield roughly an order of magnitude larger compared to helium. This implies that any argon that enters the source chamber during or after the frosting process, an amount that should be very small or zero, causes significant sputter damage.

4.2.2 Evaporation

Evaporation is a mechanisms through which filament material is lost, in addition to bombardment sputtering. Models exist to determine the evaporation rate as function of temperature [33], which is presented in figure 4.2 for tungsten filaments. It can be seen that the loss rate scales strongly with local surface temperature.

One of the mechanisms of filament deterioration arises from this strong scaling between evaporation loss and temperature. Certain spots are prone to reach higher temperatures, for instance due to small diameter variations or radiative self-heating near corners and bends. In these high-temperature spots the filament can be subject to thermal deformation and the material loss rate becomes large, rapidly decreasing the diameter. With smaller diameter resistive heating then increases, raising the local temperature further. This creates a vicious circle that can eventually lead to a filament completely snapping into two as shown in the photograph of figure 2.4.

5. Novel ion source design

- *Develop a scaled-down version of the CLPS ion source capable of steady-state operation and diagnostical flexibility.*

In this chapter, the design of the novel beam ion source is presented. In order to fulfill the purpose of facilitating both the insulation breakdown study presented in this thesis as well as more general beam source research and development, the source was designed and built to replicate the geometry and workings of the CLPS sources as best as possible. This chapter primarily serves as an overview and operational reference for the experiment, and some additional photos and descriptions have been incorporated into Appendices A and B.

5.1 Design considerations

- *What are the main design goals of the novel miniature source?*

General Neutral Beam ion source design criteria by Kunkel [14] were discussed in section 3.1. For the purpose of research and development there are some other desirable requirements, namely steady-state operation and suitable scaling considerations. These will be discussed in this section.

Steady-state operation

Regular beam shots at DIII-D last for a number of seconds, with the source operating slightly longer than that. This has the purpose of obtaining a plasma density and temperature equilibrium before the acceleration grids are engaged and the neutral beam is injected into the plasma, which improves stability and reduce fluctuations. Therefore the ion source operates for up to ten seconds at a time. This is not desirable for the purpose of testing on the miniature ion source, where a large number of discharges would have to be performed for it to match the total operational duration of the CLPS devices. If the miniature source is in continuous operation, it can be exposed to a thousand shots worth of source operation in the timespan of hours.

Scaling

Scaling is an important consideration because the miniature source will be used to conduct studies and suggest improvements for CLPS. The novel source is therefore a geometrically scaled-down version of CLPS. As found in section 3.4 various parameters, such as primary electron density fraction and ion density, are functions of the ratios between filament and anode area ratio, and plasma volume. In terms of volume it was decided that a miniature source volume of 2.3 L, cylindrical in shape, would be of suitable proportions. This volume is approximately 25 times smaller than that of CLPS. The volume can further be adjusted by moving a plasma-limiting dummy grid back and forth (see figure 5.1), which acts as a fake acceleration grid.

Diagnostical flexibility

Diagnostics lay at the foundation of plasma research and source research and development. It is therefore desirable to facilitate a flexibility in diagnostization, where various systems can be used in a number of flexible locations and can rapidly be interchanged. This is in contrast to the diagnostics on the CLPS source, which only contains a small number of fixed Langmuir probes at the acceleration grid.

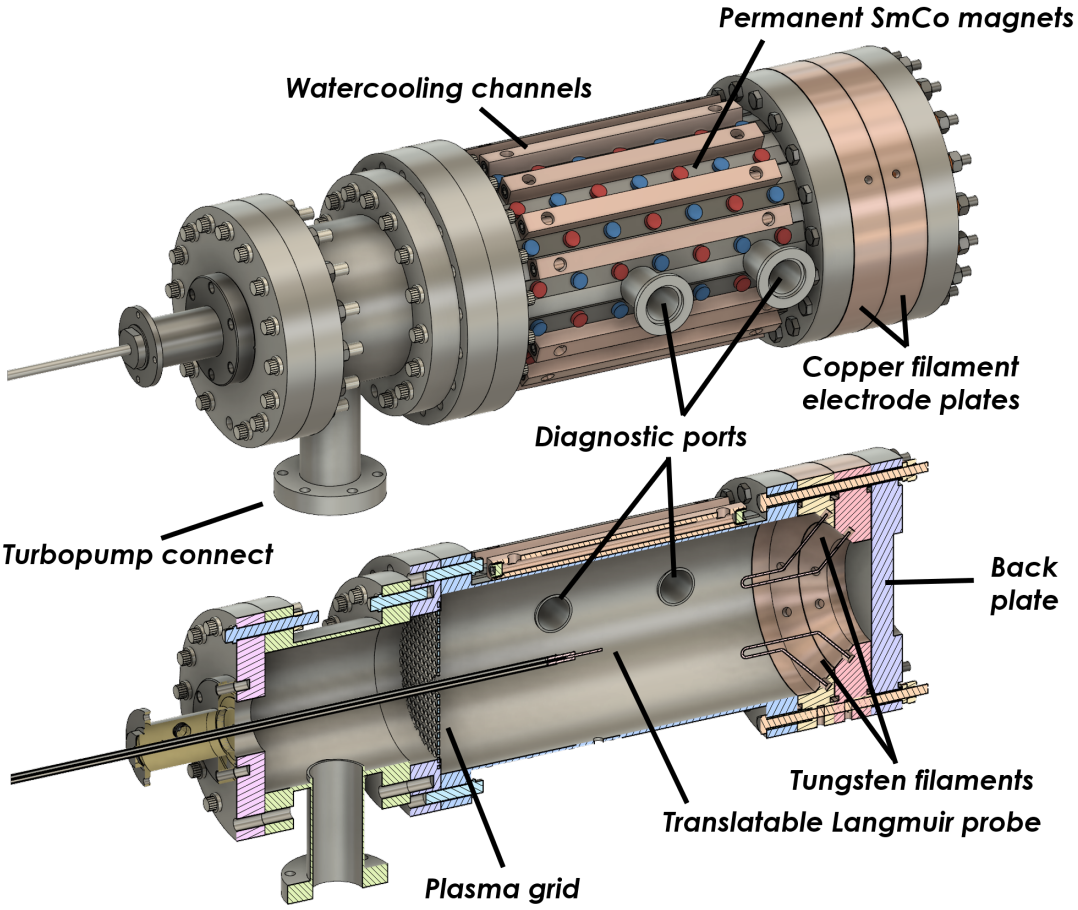

Figure 5.1: Digital (CAD) design of the new ion source with annotations. The chamber volume is approximately 2.3 L, with a diameter of 5 inches or 12.7 cm. A more detailed view of the cathode-end of the the source was shown in figure 2.5.

5.2 Main components

- *What are the main components of the novel source and what is the reasoning behind the design choices?*

In figure 5.1 an annotated overview of the components of the novel source is shown. The vacuum compartments consist of the main chamber and the auxiliary chamber, which connects to the pumping system. The cylindrical main chamber encompasses the plasma volume, which is limited on the right-hand side by the copper filament electrode plates and back plate, and on the left-hand side by the plasma grid. The plasma grid can be moved up and down the central z-axis of the cylinder to allow for a variable plasma volume. This can affect the species densities and is desirable for experimentation.

The copper filament plates have internal connectors that support up to 4 filaments simultaneously, see also figure 5.3. This can be utilized during filament deterioration studies involving a larger number of filaments running at reduced power, which may improve filament lifetime. Each filament configuration can be installed with rotational symmetry.

On either side of the main cylindrical chamber there are two ports with a direct line-of-sight to the plasma, perpendicular to the axis of the chamber. Additionally, one large flange on the far side of the chamber (left hand side, figure 5.1) is available for diagnostics. If a port is unused it can either be capped off with a blank flange or converted into a window, see the right port of figure 5.2.

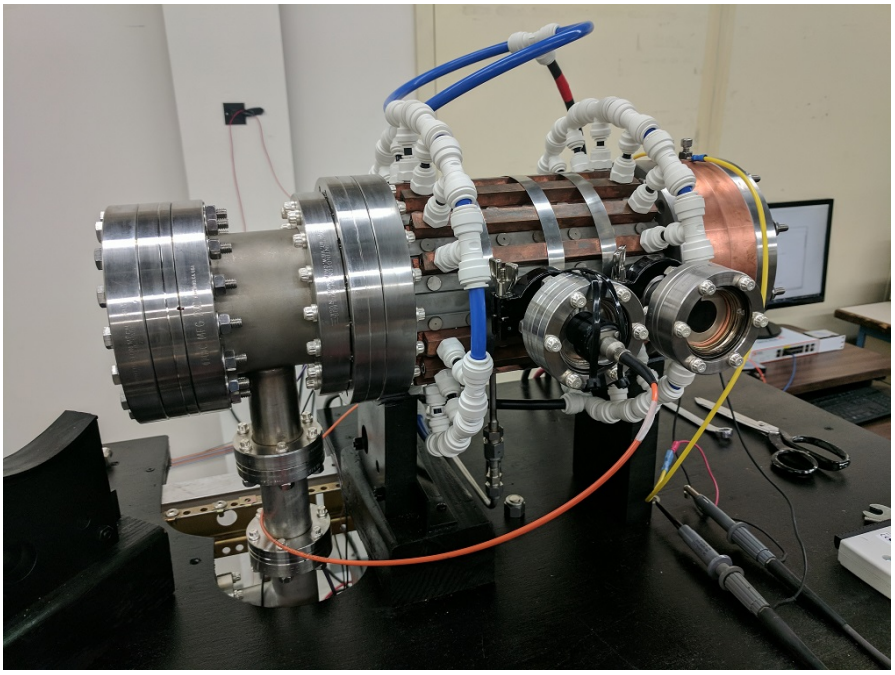

Figure 5.2: Photograph of the entire source. The left port on the facing side is connected to a collimator that sends collected photons over an optical fiber to a spectrometer. The port on the right is a window for visual inspection during discharges. The blue lines and white connectors are part of the watercooling system.

5.2.1 Confinement magnets

Certain permanent magnet configurations can be used to create plasma confining magnetic fields. Initially a checkerboard pattern is utilized, where magnets alternate in polarity both along the length and along the circumference (see figure 5.3). The magnets attach to the chamber magnetically and are fixed in the correct place by a strip with holes that is spot-welded to the outside of the chamber. The configuration can be changed by rearrangement of the magnet polarizations, or the addition and/or removal of individual magnets. Alternative configurations can be applied, for instance the filter field or supercup field. An effect of these configurations is the enhancement of the monatomic fraction, thus increasing the beam efficiency related to Requirement 5.

Permanent Samarium-Cobalt (SmCo) magnets are chosen for their high heat resistance. The magnets are cylindrical in shape with a height of 5 mm and a diameter of 10 mm. The specific material type is YXG-28, which has a demagnetization temperature of 570° K and a magnetization of ≈ 750 kAm^{-1}. A Neodymium magnet with similar dimensions has a demagnetization temperature of 350° K and a magnetization of ≈ 900 kAm^{-1}. Samarium-Cobalt was chosen because the higher temperature resistance was deemed desirable.

The field strength of the chosen magnets is 3000 G, resulting in a maximum cusp strength of 2000 G due to finite wall thickness. This is identical to the multicusp field in the CLPS design, and sufficient to regard the plasma as magnetized in the cusp region. The field strength can be further altered by replacing or stacking magnets. The addition of a ferromagnetic bar on the outside of the magnet arrays can also increase the field strength inside the chamber, as it would suppress the external field lines.

5.2.2 Vacuum

The vacuum subsystem contains of a roughing pump (Varian SD-80) and a turbopump (Pfeiffer TPU 170). Vacuum pressures a low as 10^{-6} mTorr can be achieved in the source, lower than those of CLPS (see the Glossary for SI conversions). This is indicative of a relatively low impurity presence during typical operation in the range of 1 to 100 mTorr.

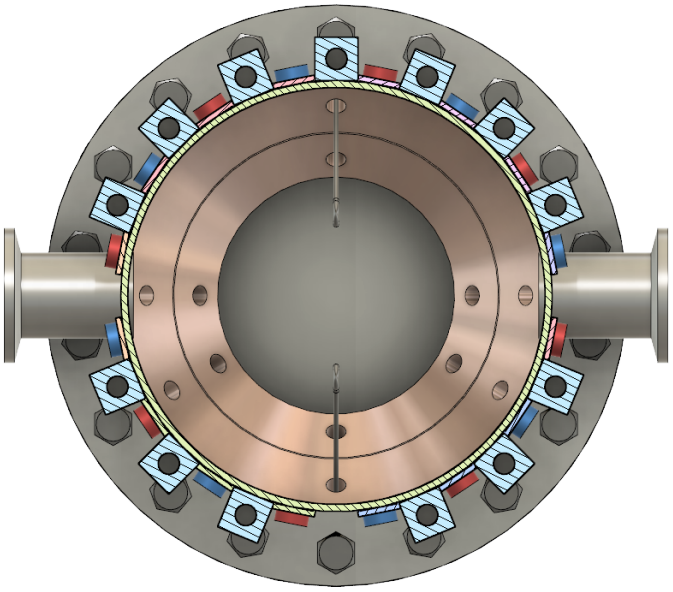

Figure 5.3: Cross-section of the CAD design showing the magnet checkerboard pattern and water cooling lines. The alternating polarity of the 16 permanent Samarium-Cobalt magnets along the circumference is indicated by color. In this configuration two filaments are shown.

5.2.3 Electrical

Power is supplied to the plasma by the electrical system and its design and properties greatly affect the characteristics and performance of the source. The electrical system heats the filament(s) to emissive levels and drives the potential drop between the cathode and anode from which primary electrons gain their energy. Therefore two independent supplies are required; the *filament power supply* and *arc power supply*. Generally speaking, the filament power supply is low potential and high current, whilst the arc power supply is high potential and low current. Since the filament power supply is connected directly to both cathode plates it floats at arc voltage. This can be seen in figure 5.4

The filament power supply is DC. An AC power supply can also be used, but DC was chosen based on availability and similarity to CLPS. Details of the arc and filament power supplies can be found in table 5.1.

Table 5.1: Main parameters of the power supplies.

Parameter	Arc supply	Filament supply
Manufacturer	Electronic Measurements Inc*	Keysight Technologies
Type	ESS 160-62 Power Supply	6031A
Voltage output	160 VDC	20 VDC
Current output	62 A	120 A
Rated output power	10 kW	1 kW
Steady-state	yes	yes
Remote control capability	yes	yes

* Now TDK-LAMBDA.

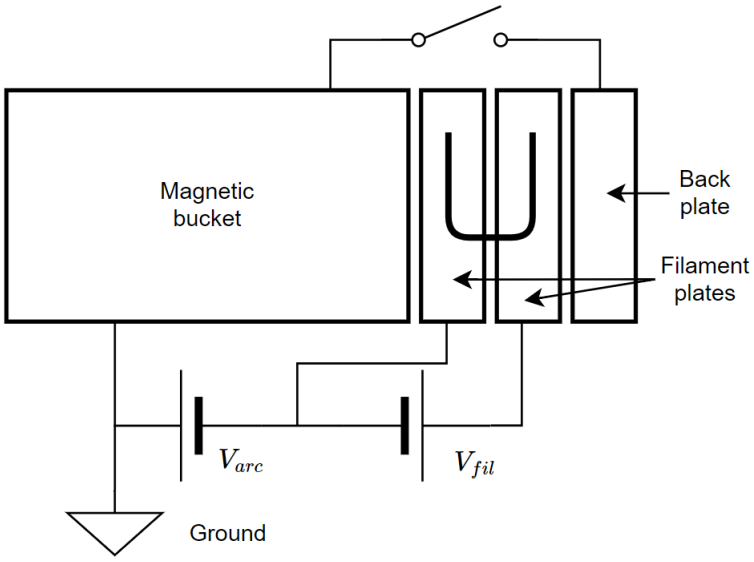

Figure 5.4: Diagram of the electrical system. In this configuration the chamber is at ground potential for safety reasons, thus the arc power supply drops the filament power supply and cathode down to minus arc potential. The filament power supply is connected directly to the filament plates, which are interconnected by the filament(s). The back plate can be connected to either electrode or kept floating, depending on the experiment.

5.2.4 Cooling

- *How is steady-state operation achieved?*

As was described previously steady-state operation is one of the goals of the novel beam source, specifically for long-duration testing purposes. During short discharges ($\leq$ 10 s) the released heat is manageable. In contrast, during steady-state operation some components reach damaging temperature levels and thus require protective systems. Thus, the cooling system has the task of dissipating heat generated during the discharge and reducing the temperature of the vacuum chamber. The primary reason is the protection of the magnets, that can lose magnetization permanently if a critical temperature is reached or exceeded. For Samarium-Cobalt this is 570° K (see section 5.2.1). Furthermore, components such as rubber vacuum seals have to be thermally protected and operator safety is a concern.

A watercooling system was designed that extracts heat from the chamber walls using a flow of chilled water. The system consists of a high-rate pump and chiller unit (see table 5.2), which is connected to the setup with flexible water lines. Distilled water is ran along the chamber walls in a zig-zag pattern through 13 square copper tubes, visible in figure 5.3. Copper is chosen for its relatively high heat conductivity. Heat extracted from the system consequently causes a temperature increase in the coolant, which is ultimately dissipated in the chiller unit.

Table 5.2: Main parameters of the cooling system.

Parameter	Value
Manufacturer	NESLAB*
Model	HX-150 (pump type PD-2)
Coolant	Distilled water
Cooling capacity	4 kW
Flow rate	13.2 L/min
Remote control capability	no
Configuration	13 lines, zig-zag

* Now Thermo Scientific.

The copper lines carrying the coolant are clamped against the chamber walls. Between the chamber surface and the lines is a thin layer of so-called copper sponge. This serves two functions.

Firstly, due to the curvature of the chamber wall the square copper lines do not transfer heat efficiently. The copper sponge compresses and increases the conducting surface area, increasing cooling efficiency. Secondly, the copper foam prevents damage to the chamber wall as the cooling channels are clamped very strongly.

5.3 Diagnostics

- *What diagnostics aid in the plasma characterization and insulation breakdown studies?*

Several diagnostical systems collect data during a discharge and return essential parameters that provide insight into the physical processes. This is essential for the plasma characterization process, insulation breakdown investigation and any further studies. Multiple electrical sensors provide critical discharge parameters such as current, voltage, and several filament properties. A movable Langmuir probe provides plasma parameters as a function of time and space that are used to characterize and compare the plasma in light of the theory and beam source requirements (section 3.1). Because low ion temperature is an important criteria (see Requirement 4) spectral measurements are obtained with optical spectrometry that provides ion species densities and temperatures. Below an overview of these systems is presented, followed by a brief discussion of proposed diagnostics and improvements.

5.3.1 Electrical sensors

- *How can electrical parameters be measured accurately?*

The arc and filament power supplies (see table 5.1) provide voltage and current sensing terminals, but these values do not necessarily correspond with the values measured directly on the chamber. Moreover, it was found that the signal outputs of the sensing terminals are at arc voltage during operation. It is undesirable to read these high-potential signals directly with a data acquisition instrument for safety and practical reasons. Therefore several other methods were used to obtain the electrical parameters of the discharge.

Voltages

Voltages are measured directly at the cathode and anode by utilizing DC voltage downstepping circuits. In these circuits two parallel resistors of different magnitudes cause a 100-fold drop in signal potential. Hence the arc voltage is reduced to a signal within in the range of $0.00 - 1.60$ V, which is fed into a Data Acquisition system (DAQ). The arc voltage is measured between the anode (ground $\frac{\perp}{=}$) and the negative filament plate. The filament voltage is obtained similarly, but instead the difference is taken between the positive and negative filament plate, with respect to $\frac{\perp}{=}$. As a consequence the uncertainty in the filament voltage is twice that of the arc voltage.

Currents

The currents through the leads attached to the arc chamber are measured with LEM® current transducers. These provide high accuracy and a wide range. Each transducer outputs a voltage signal which is read by the DAQ. Especially the arc or discharge current is an important diagnostic, as it correlates directly to the output performance of the beam source.

Inferred filament properties

The resistivity of the filaments is temperature-dependent [34]. Thus by obtaining the filament resistance with

$$R_{fil} = N\frac{V_{fil}}{I_{fil}}, \tag{5.1}$$

where N is the number of filaments, the temperature can be found. The equations for thermionic emission, 3.2 and 3.3, can then be used to yield the thermionic emission current density J_{em}.

5.3.2 Custom Langmuir probe

- *How is the Langmuir probe diagnostic designed?*

Swept probe analysis is a key tool for obtaining estimates of the physical parameters of a plasma. Parameters that can be acquired include potentials, densities, the electron temperature and the Electron Energy Distribution Function (EEDF). The operating principle is the collection of charge from the plasma on the surface of a probe during a voltage sweep. Such a probe is called a Langmuir probe [35]. The theory of Langmuir probe analysis is extensive and will not be discussed in full detail here for brevity.

For the purpose of plasma characterization a custom Langmuir probe was constructed, as shown on the right hand side in figure 5.5. An overview of the properties can be found in table 5.3. It consists of a stainless steel tube fed through a vacuum compatible rotary-linear motion manipulator. A small hole is punctured in the tube wall to allow the inner volume to drop to vacuum pressure. An insulated wire is fed through this tube and connects to the tungsten probe tip on the vacuum side. The probe tip is cylindrical in shape and has a total plasma-exposed surface area of $S_p = 7.6$ mm^2. The tip is pressure-fit inside a Macor holder attached to the end of the tube. Macor is a machinable, temperature resistant ceramic. A handle is attached to the other end of the tube for easy manipulation. A small electrically insulating vacuum feed-through allows the wire carrying the probe current to exit the setup.

The probe position is recorded based on a start and end position given a certain discharge time. From this the position at each moment of time can be obtained. However, this requires the translation speed to be constant. Vacuum grease is applied to the probe shaft but this does not result in a constant level of friction along the total length. Thus if a constant force is applied on the handle (for instance during manual linear motion) the translation speed of the probe tip will vary. Instead a threaded rod of similar length to the tube is positioned adjacently. By using an electric drill to rotate the rod at a constant rate with a bracket connecting the threaded rod and the handle, the motion will be of constant speed.

A typical $I - V$ characteristic is shown in figure 5.6. The raw signal is obtained after amplification. An amplification factor of 100 is applied to increase the resolution of low current signals, especially the ion saturation region, and a factor of 10 in the other region. As figure 5.6 shows there exists some periodic noise in the raw signal. Without any filtering the first and second derivatives contain too many inaccuracies to be used, as any noise in the raw signal becomes amplified. It is shown that the noise can be eliminated by applying a digital Butterworth filter [36] with a cutoff frequency of 30 Hz. The filter is applied in a forward-backward manner, preventing undesirable phase shift. It is implemented in Python with an order of $N = 2$. This order was empirically chosen. As a result the response of the filter is smooth and periodic noise is no longer present. The error in the signal can be reduced further by averaging over a number of $I - V$ curves, but this is presently not implemented.

Figure 5.5: Photograph of the fully assembled Langmuir probe. The probe tip and housing tube are fed through a so-called vacuum-compatible rotary-linear motion manipulator.

Table 5.3: Parameters of the custom Langmuir probe.

Parameter	Value
Type	Single
Geometry	Cylindrical
Probe dimensions	⌀1.57 by 1.15 mm
Probe material	Tungsten
Housing material	Stainless steel
Insulation material	Macor*
Swept voltage	±30 V (sawtooth wave)
Maximum current	100 mA**
Distance	$0 - 30$ cm
Orientation	Axial or radial

* A machinable, heat-resistant ceramic by Corning Inc.
** Prior to registration the current signal is split into two and amplified by 10 and 100 times. This enhances the resolution of the electron and ion saturation regimes, respectively.

Analysis of the probe characteristic

Obtaining the physical plasma parameters from a $I - V$ curve such as the one shown in figure 5.6 is implemented in Python. The initial step is data preprocessing. This includes extracting a single sweep from the sawtooth profile, correcting for signal amplification and external wire resistance, and applying the Butterworth filter as described. From the filtered signal the floating and plasma potentials are immediately obtained: V_F and V_P, respectively [35]. The floating potential originates from the potential at which the ion and electron current cancel out and $I = 0$. The plasma potential is taken as the potential at which the second derivative $\frac{\mathrm{d}^2 I}{\mathrm{d}V^2}$ is zero, which is roughly where the current begins to deviate from exponential growth. Rough estimates of the saturation current densities $j_{s,i}$ and $j_{s,e}$ for ions and electrons, respectively, are also obtained.

An exponential fit of the electron accumulation region between the floating and plasma potentials provides an estimate of the *electron* temperature T_e. This exponential fit is a correct assumption as long as the plasma is Maxwellian. Knowing the electron temperature the approximate ion and electron densities, n_i and n_e, can be calculated. Here a collisionless sheath is assumed, which is valid in the relevant low density regime.

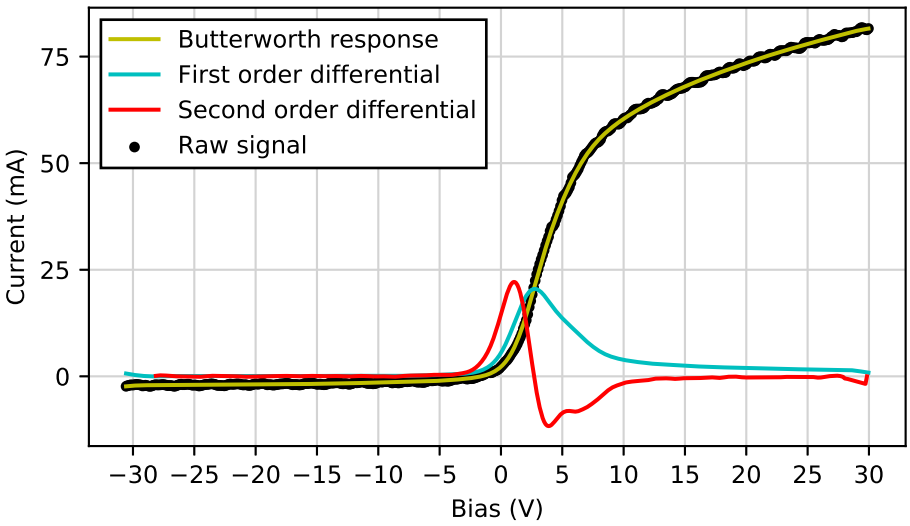

Figure 5.6: A sample obtained Langmuir $I - V$ curve is shown. To remove the noise from the raw probe data a forward-backward Butterworth filter [36] is applied digitally. The first and second derivatives of the filtered signal are relatively smooth (shown unitless).

As a final step in the analysis Orbital Motion Limited (OML) theory is applied to provide a more accurate reading of the ion density [37]. The advantage of OML theory is that there is no dependency on the previously obtained electron temperature, under the assumption of an absence of electron-ion collisions in the probe sheath. Allen-Boyd-Reynolds (ABR) and Bernstein-Rabinowitz-Laframboise (BRL) theory are also considered, but it is found in literature that compared to OML theory these underestimate and overestimate the ion density, respectively [38]. The ion accumulation region ($V < V_F$) is fit to the ion current I_{OML}, which is given by

$$I_{OML} = 7.05 S_p n_{i11} \sqrt{\frac{e\,(V_P - V)}{M_i}}, \tag{5.2}$$

where n_{i11} is the ion density in 10^{11} cm^{-3}, S_p the probe area in cm^2, and M_i the ion mass number.

5.3.3 Optical spectroscopy

The use of spectrometers to obtain plasma line spectra has multiple purposes with respect to both experiments conducted during this work and ones that are proposed. It can be used for the detection of impurities in the plasma that originate from outgassing, vacuum seal leaks, or filament material loss. Furthermore, the presence of various ion species can be quantified and compared, which is especially important considering the desire for a high monatomic fraction in beam sources (see section 3.1, Requirement 5).

Bundles of optical fibers attached to diagnostical windows lead to two spectrometers, an Ocean Optics JAZ and an Ocean Optics USB4000. These provide spectra in the range of 430-1100 nm ($\Delta\lambda = 0.36$ nm) and 400-525 nm ($\Delta\lambda = 0.044$ nm), respectively. These combined ranges are sufficient to capture most spectral lines of the described species. However, due to the low ion temperatures Doppler broadening is relatively weak. Assuming an ion temperature of 0.2 eV the relative FWHM equals $\frac{\Delta\lambda}{\lambda} = 1.7 \cdot 10^{-5}$. Therefore a higher spectral resolution is required to accurately measure the ion species temperatures.

5.3.4 Proposed diagnostics

Several other diagnostics have been proposed for use in the continuation of the studies presented in this work and in other future experiments. As was discussed in the previous section, ion temperatures are relatively low and optical spectroscopy is unable to obtain accurate results in the current implementation. Especially in light of the need for low ion temperature (see Requirement 4), a method to obtain the Ion Energy Distribution (IED) in the source is highly desirable. Such measurements could be obtained with a Retarding Field Energy Analyzer (RFEA), ideally placed near the exit grid. Mass spectrometry is available on-site and could provide additional information on the gas mixture. Weak lines from sputtered cathode metals such as tungsten and copper are lost due to optical oversaturation caused by the intense filament emission, but could be detected with the use of mass spectrometry. Furthermore, an improvement upon the acquired EEDF could be made by implementation of the Boyd-Twiddy method [39]. This method employs a modulated signal to remove the need to acquire the second derivative of the Langmuir probe characteristic, a step that generally introduces a significant error.

In the future an expansion of the source is planned, will would add an extraction grid in order to produce a small ionic beam, firing into a calorimeter. This will further increase the experimental capability of the source, enabling studies involving beam optics and beam performance for CLPS.

6. Confinement validation

- *Validate the confinement properties using computational modelling.*

There is a need for validation of primary electron confinement properties due to the novel chamber geometry, cusp grid spacing and magnet strength. In order to validate this a computational study was conducted in parallel with the source development. Particle tracing can be implemented computationally and trajectory simulation of a large number of particles can give an indication of confinement properties. Since no exact definition of satisfactory confinement is defined, the validation will be qualitative of nature.

6.1 Model

- *What are the model and assumptions?*

A 2D model with rotational symmetry could be used to obtain the magnetic field. However, the particle tracing requires a fully 3D model. Therefore a 3D, digital model of the chamber was constructed in COMSOL MultiPhysics™ [40], provided by H. Torreblanca of General Atomics. This model, based on the CAD design shown in figure 5.1, contains only the source chamber, the magnet strip and permanent Samarium-Cobalt magnets. The electromagnetic field is calculated as if in a vacuum, and no coupling between the subsequent traced particles and field is incorporated. The effect of the primary electrons on the structure of the magnetic field is negligible.

Furthermore, no particle collisions of any kind were incorporated in the model. This simplification was made because collisions reduce the primary electron energy, which consequently become more prone to reflection off the surface fields. Thus, from a confinement perspective, a worst-case scenario applies in terms of primary electron energies.

6.2 Computational results

6.2.1 Magnetic field strength

- *What is the strength and structure of the multicusp field?*

From Maxwell's equations follows the magnetic field structure of the confinement cusps, as can be seen in figure 6.1. The field is evaluated in the full 3D volume, and a slice halfway along the central axis of the chamber is shown.

The maximum field strength in the chamber is approximately 2000 G, smaller than the magnet surface field of 3000 G due to the finite thickness of the chamber wall. The stainless steel walls are weakly paramagnetic and thus absorb some of the field lines going into the vessel, reducing its strength. In figure 6.1 it can be seen that cusps of similar absolute field strength form at the location of each permanent magnet. The field structures protrude into the plasma with diminishing strength (see also the field strength magnitude contours, figure 6.2). Near the center the alternating polarities cancel out and the absolute field strength is less than 0.5% that of the edge field (ie. < 10 G). This agrees with the operational principle of multicusp confinement proposed by Moore [22]; primary electrons are released inside a volume of weak magnetization and thus reflected off the stronger surface fields.

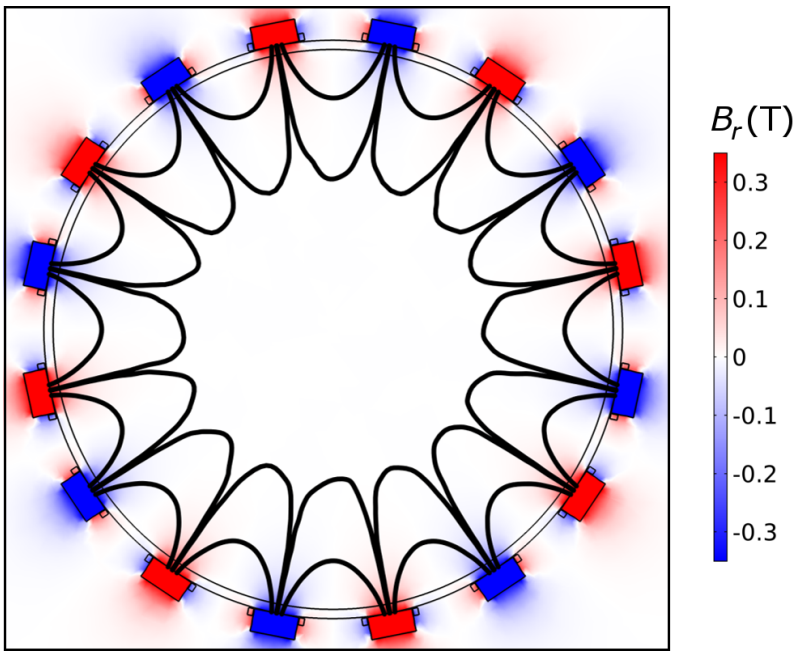

Figure 6.1: Magnetic field strength and field lines inside the chamber. The field radial strength B_r is shown (in Teslas). The red-blue coloring indicates the sign of the radial field, which is shown to be of arbitrary alternating polarity. Black lines indicate the cusp field lines at various positions.

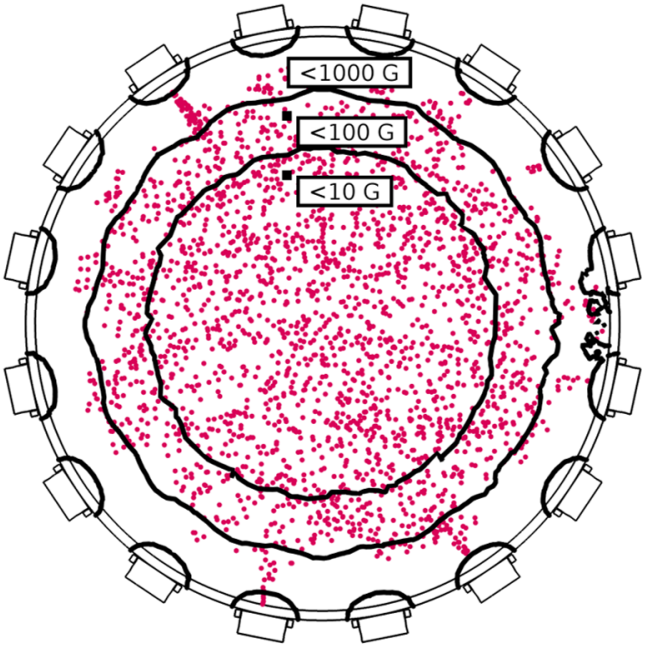

Figure 6.2: Poincaré plot of primary electron trajectories with magnetic field strength contours. Trajectories mostly stay within the low-field contours.

6.2.2 Primary electron confinement

- *Are primary electrons confined by this cusp configuration?*

$N = 10^4$ electrons are released into the model volume at $t = 0$ s and their positions are traced. They originate from the filaments and are given a monoenergetic velocity perpendicular to the surface of a typical 80 eV. The trajectories are then calculated for a duration of 45 ns, with picosecond timesteps. Small timesteps are necessary due to the high primary electron velocity.

The end result of this simulation can be seen in the Poincaré plot of figure 6.2. The contours of the radial magnetic field strength show a diminishing strength towards the center, which agrees with the design principle of multicusp confinement fields. Qualitative assessment of the particle tracing result can conclude that, at least in this general case, the majority of the primary electrons are contained within the < 100 G field strength contour, and thus satisfy the condition of confinement; reflection off surface fields increases the expected path length of energetic electron beyond their ionization mean free path, which was approximated to be 47 cm in section 3.3. Since the geometric model is rotationally symmetric in an ideal result every cusp should be identical. However, near specific cusps, such as the second left of the top and the second right of the bottom, electrons can be seen to get close and appear to lose confinement. This could be a consequence of computational aberrations in the calculated field structure, such as can be seen on the right-hand field contours of figure 6.2, or a timestep that was chosen too large.

7. Ion source plasma characterization

- *Characterize the plasma parameters and operational modes of the new ion source and compare the results with theory.*

The purpose of characterization is to obtain knowledge of important discharge parameters and their behaviour, to serve as experimental validation of the theory presented in chapters 3 and 4, and to check the performance in light of the ion source requirements presented in section 3.1. Primarily, this characterization will focus on three aspects of source operation relevant to NBI criteria and performance. The first step is to identify what parameters of the discharge can be changed, and within what range.

7.1 Experiment operation

7.1.1 Parameters

- *What are the experimental knobs?*

Experimentally there are several ways to change the properties of the ion source plasma. An extensive overview of these is presented in table 7.1. An important distinction to be made is whether or not a parameter can be changed during an experimental discharge. If this is the case the parameter has the designation *dynamic*.

Table 7.1: This table presents parameters that can be changed to affect the properties of the plasma, ie. 'knobs' of the experimental setup. The fields *Symbol*, *Parameter*, and *Range* introduce these parameters and their scope. The field *Dynamic* indicates parameters that can be adjusted during a single discharge. The *CLPS* field provides a comparison with the large-scale ion sources.

Symbol	Parameter	Range	Dynamic	CLPS
V_{arc}	Arc voltage	0-120 V	yes	60-120 V
I_{arc}	Arc current	0-30 A	yes	580 A
I_{fil}	Filament current	0-100 A	yes	0-3000 A
p_0	Background pressure	1-100 mTorr	yes*	25 mTorr
-	Pulse length	steady-state	yes	0-10 s
-	Operating gas mixture	H, He, Ar**	no	H, D, He
A_{ic}	Cathode area†	-	no	-
N_{fil}	Number of filaments	1-4	no	32
N_c	Number of cusps	0-98	no	-
B_{pm}	Permanent magnet strength	-	no	3000 G
-	Confinement field shape	Multiple patterns‡	no	Checkerboard

* Due to technical issues the pressure could not be precisely regulated through a mass flow controller, requiring manual valve control instead. As a result there can be pressure fluctuations of $\approx \pm 5$ % over the duration of a shot, in a worst case scenario.

** Up to two gas bottles can be connected simultaneously. Many gases are available, but may require require paperwork or additional safety requirements.

† The cathode area can be increased by changing the electrical configuration of the back plate. This can be connected to the cathode, anode, or kept floating.

‡ Any configuration can be installed: checkerboard, line-cusp, filter field or supercusp, etc.

Dynamic variables can be regulated electrically, such as through arc and filament power supply settings, or through valve operation. Additionally the duration of a discharge is a parameter

that can be changed adaptively. The remaining knobs require the (partial) disassembly of the source, or require complete deactivation for safety purposes and are therefore non-dynamic.

In figure 7.1 the new ion source is shown during a helium discharge. Hydrogen, as well as argon, gas bottles were also installed but not used in the source during the work presented in this thesis. The reason is that due to technical issues with the flow controllers multi-gas operation was unattainable, and safety restrictions required special procedures regarding hydrogen operation. In the photographs the bright light originates from the hot cathode and drowns out plasma lines to the naked eye. To prevent spectroscopic oversaturation care has to be taken that the spectrometer is never pointed directly at the filament.

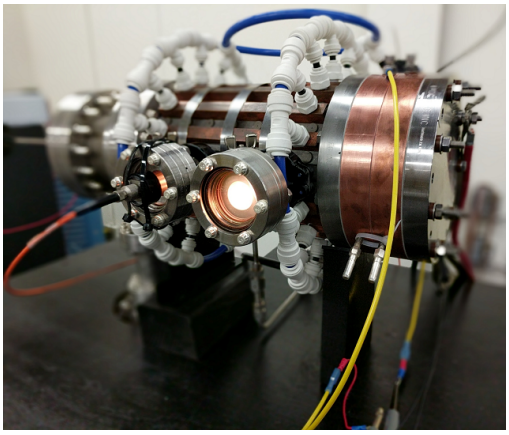

(a) Entire arc chamber and surrounding watercooling lines. The copper filament plates can be seen on the right hand side. The yellow wires are part of the voltage sensor system. Two of the four diagnostic ports can be seen, one of which connected to a spectrometer.

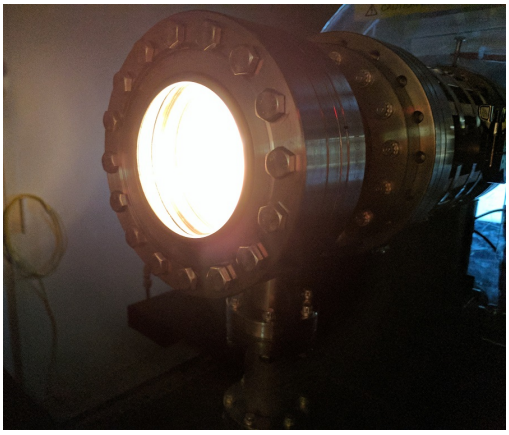

(b) View of the far-side of the ion source (left hand side of figures 7.1a and 5.1). In this configuration the Langmuir probe is attached to the side of the chamber and a large window provides a view into the source.

Figure 7.1: Photographs of the table-top beam source during operation.

After brief discussions of obtained measurements and waveforms the next sections will present steps of the characterization process. These involve altering the parameters previously presented and discussing the corresponding effect on the discharge plasma characteristics. The parameters involved are mostly dynamic, as these are least time intensive and results can be obtained rapidly. Since many different beam source parameters and properties can be characterized the study presented in this work will focus on three relevant aspects: the behaviour of arc current in the operational modes, which corresponds directly to source performance, the existence of non-Maxwellian electron populations, and the spatial plasma uniformity, which is one of the main beam source requirements.

7.1.2 Discharge waveforms

- *How is a typical source discharge waveform interpreted?*

Figure 7.2 shows some of the waveforms of a typical discharge in the new ion source. An arc voltage of 76 V is applied at $t = 2$ s and turned off at $t = 44$ s. During operation the voltage is ramped up to 116 V, starting at $t = 12$ s. The filament power supply, which is current-limited to $I_{fil} = 108$ A, is engaged prior to the start of the shot in order to let the filament reach thermal equilibrium. If the filament is still heating up during the data collection process this may lead to false conclusions. Similarly the pressure is adjusted to the desired value prior to the discharge, as it also requires some time to stabilize.

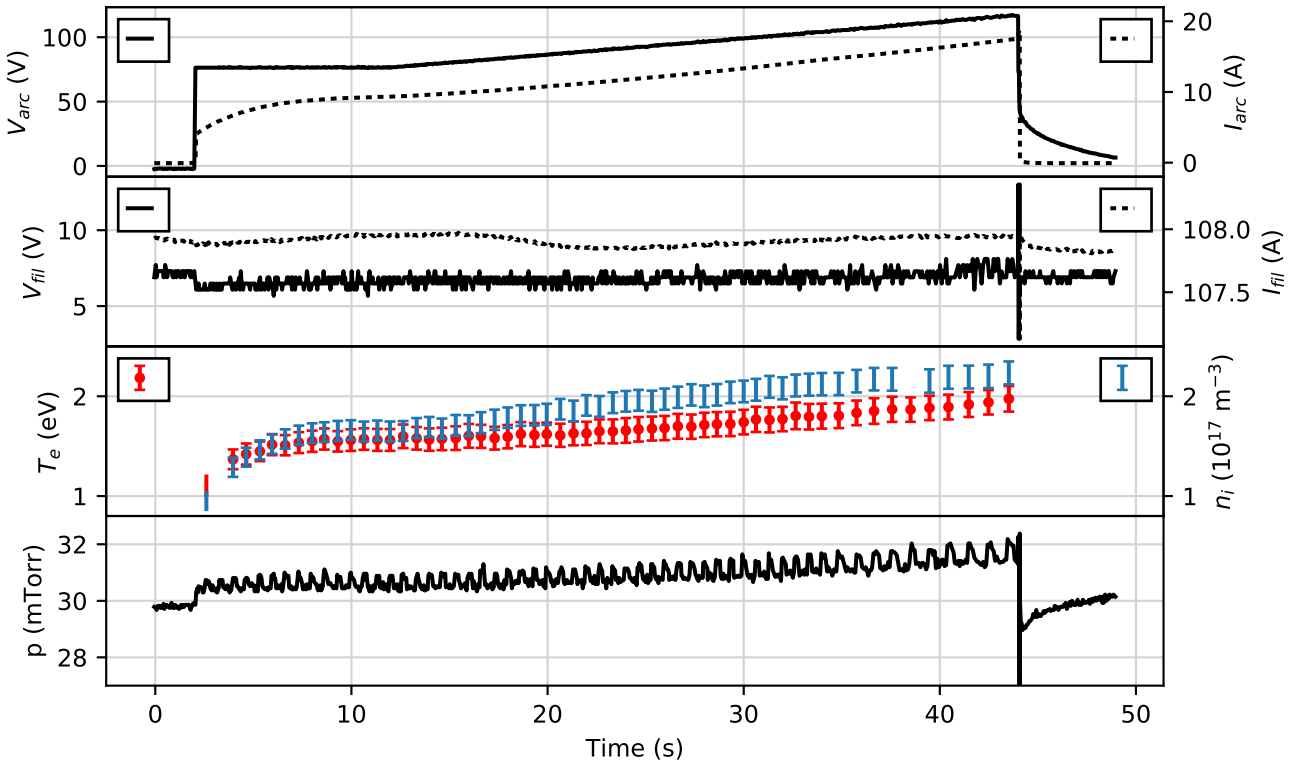

Figure 7.2: Typical discharge waveforms (discharge #4, in helium). It shows the arc and filament electrical parameters, electron temperature and ion density obtained from the Langmuir probe, and the pressure as a function of time. The obtained Langmuir parameters contain error bars that follow from the probe characteristic fits.

Parameters acquired from Langmuir probe analysis cannot be obtained until the presence of a plasma. Initially the obtained electron temperature is approximately 1.5 eV and the ion density $1.8 \cdot 10^{17}$ m^{-3}, and rise to 2.0 eV and $2.4 \cdot 10^{17}$ m^{-3}. Directly after appearance of the plasma the arc current rises sharply to $I_{arc} = 4.3$ A, followed by a gradual increase to an equilibrium of 9.5 A. The arc voltage ramp is not initiated until this equilibrium has been reached.

As described in table 7.1 the background pressure regulation is manual and therefore subject to increases over the duration of the shot, as the temperature in the chamber rises. The technical reason is that the lower operational limit of the mass flow controller units that regulate gas flow was too high to sustain the desired vacuum pressure. Hence a manual needle valve was used instead, at the expense of precise control.

7.1.3 Uncertainties and errors

- *What is the uncertainty in the obtained measurements?*

An important question to be answered prior to any experiment is *what is the uncertainty in the obtained measurements*? Measurement uncertainty can be manifested as systematic errors, noise-like errors and signal anomalies. These will be discussed briefly in the context of the miniature ion source.

Systematic errors arise due to erroneous assumptions or other inaccuracies in the measurement process itself. For instance, an incorrect Langmuir probe surface area will result in systematic errors in the acquired ion and electron densities, which are a function of the collected current density. To prevent systematic errors from occurring calibration with known values was performed wherever possible. This includes calibration of electrical sensors against known voltages and currents, using pre-calibrated pressure sensors, and cross-checking obtained plasma characteristics.

Uncertainty is inherent in every measured signal. The uncertainty in the voltage sensors is ±0.4 V. This absolute error is relatively small when measuring arc voltage but results in a relative error between 5 and 8 % in the lower filament voltage (see figure 7.2). Consequently this error propagates in the obtained filament resistivity, temperature, and thermionic emission. A digital Savitzky-Golay filter [41] is applied to increase the signal-to-noise ratio of the filament voltage measurement (and the corresponding derived parameters) without distortion. The uncertainties in the obtained Langmuir parameters follow from the fits of the probe characteristic. They are indicated by error bars in the waveform, with a mean relative error of 7 % for the electron temperature measurement and 6 % for the ion density.

Due to the nature of the electrical sensor configuration some parameters are susceptible to sudden changes in arc voltage, as can be seen in figure 7.2. Upon turn-off of the arc voltage ($t = 44$ s) anomalous values are registered in the filament voltage and pressure. Unlike the filament voltage sensor wire the pressure sensor is not directly connected to the arc voltage, but an indirect connection exists via terminals on the data acquisition device. During analysis care is taken that anomalies such as these are disregarded.

7.2 Discharge current

- *How does the discharge current relate to performance?*

The arc, or discharge, current is equivalent to the total loss of charged particles to the chamber (anode) walls. Assuming quasineutrality both ion and electron anode loss currents are proportional to $n_i\sqrt{T_e}$, which arises from equations 3.18a and 3.17, respectively. This is demonstrated in figure 7.3, where the discharge current is shown as function of the loss current proportionality of ion density and root electron temperature. A linear fit qualitatively indicates agreement with the expectation. Because the ideal injected beam power has an identical proportionality, see equation 2.1, the arc current is a direct indication of source performance or the effective equivalent thereof. Moreover, the arc current provides insight into the physical processes inside the ion source plasma; the discharge current is directly proportional the ionization intensity.

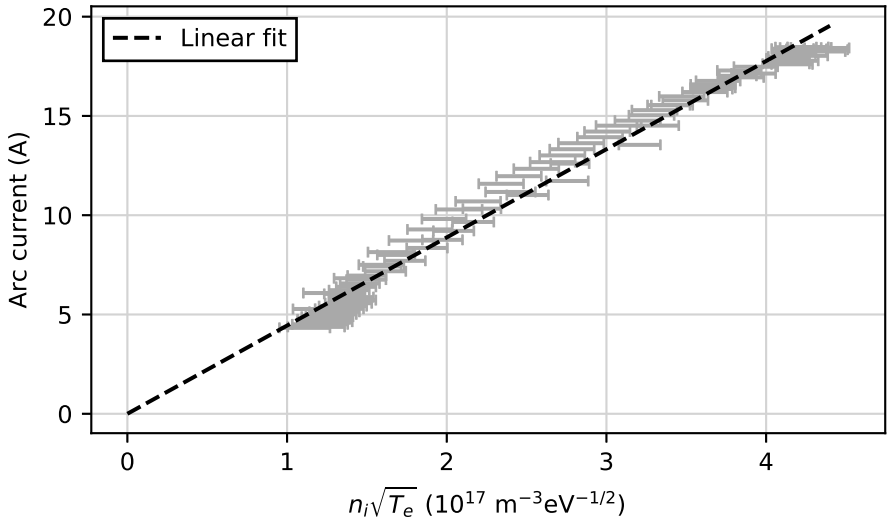

Figure 7.3: Proportionality of arc (ie. discharge) current to ion density and root electron temperature. Error bars indicate the uncertainty in the measurements. The hypothesized linear relation is indicated by a fitted line.

It can be concluded that arc current is directly correlated to beam performance. Since the arc current itself is the consequence of ionization intensity, therefore the operational modes that affect the ionization intensity greatly affect the performance of the ion source. As a consequence

the behaviour of the emission limited and space-charge limited modes, discussed in sections 4.1.1 and 4.1.2, in the new source will now be investigated and compared to theory.

7.2.1 Ionization intensity in different modes

- *How does the arc current scale with discharge voltage in the modes?*

In figure 7.4 the increasing arc current as a function of voltage is shown, which is the main mode of operation used for CLPS. A helium plasma is used. Initially the voltage is below the ionization energy and consequently the arc current is zero. After the threshold of 24.6 eV the discharge current rises, and continues to do so until the end of the voltage ramp. This can be attributed to an increase in ionization intensity, which is caused by two distinct mechanisms.

1. If the emission is not limited by the filament, an increased arc voltage will raise the space-charge limited extraction current (equation 4.9). More primary electrons are released into the plasma, causing an increase in ionization current and correspondingly discharge current.

2. The potential drop that primary electrons fall through grows, providing them with more energy. This increases the electron bombardment ionization rate $\langle \sigma_i^p v_p \rangle$ (see figure 3.3).

These two mechanisms can be summarized as *upon a raise in discharge voltage there is a greater flux of more energetic primary electrons into the chamber.*

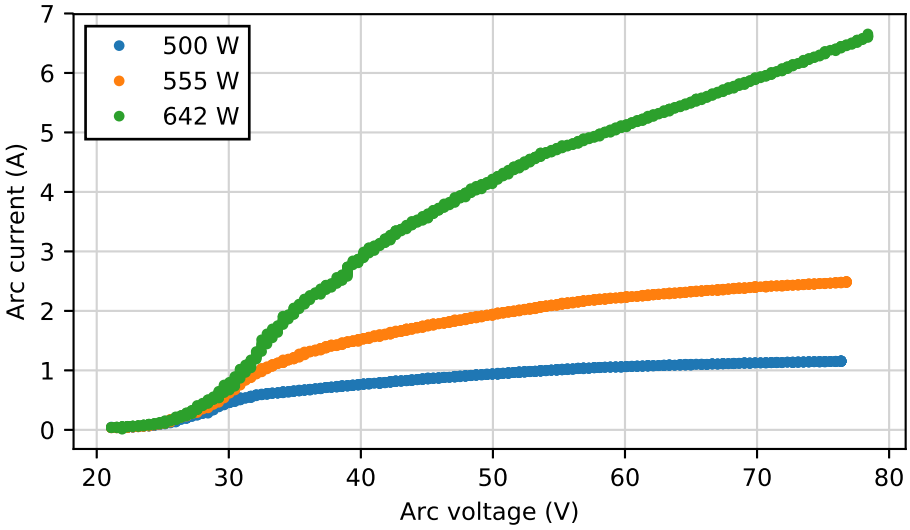

Figure 7.4: Arc current-voltage characteristic curve during a voltage scan for three different filament powers. The experiments are performed in helium at $p = 75$ mTorr. The significant differences in discharge current for a given voltage arise from the differences in thermionic emission, which scales strongly with filament power or temperature.

The individual mechanisms can be isolated based on their proportionality. If the source is in the space-charge limited mode the discharge current is expected to scale linearly with $\sqrt{V_{arc}} \langle \sigma_i^p v_p \rangle$, which follows from the two mechanisms described previously. On the other hand, if the primary electron current becomes limited by thermionic emission the first mechanism no longer applies and the proportionality to solely $\langle \sigma_i^p v_p \rangle$ should hold. This proportionality isolation is experimentally demonstrated, see figure 7.5.

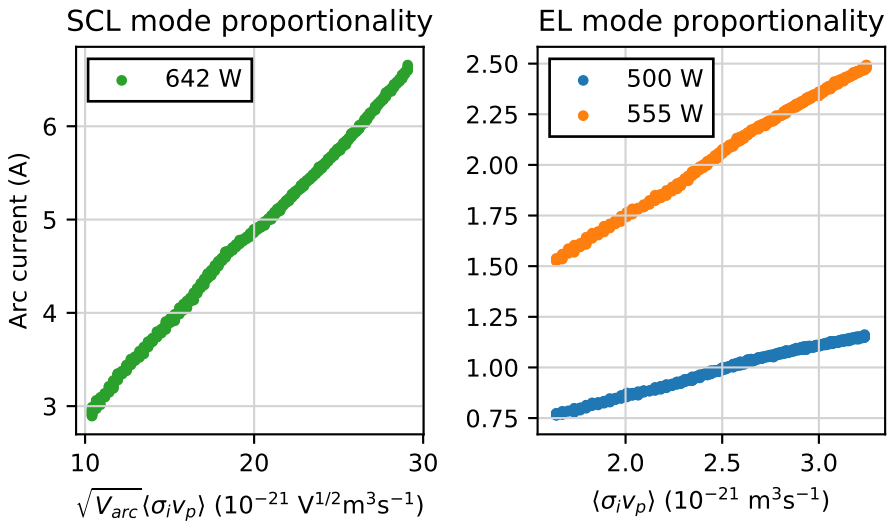

Figure 7.5: This figure shows the isolation of the two discharge current operating modes with data from figure 7.4. On the left hand side the high filament power case is shown, which is expected to operate in the space-charge limited (SCL) mode. The corresponding proportionality is $\sqrt{V_{arc}}\,\langle\sigma_i^p v_p\rangle$, which seems to agree with experimental results. On the right hand side the lower power cases are shown. It can be seen that these operate in the emission limited (EL) mode, as in these situations the arc current appears to be directly proportional to solely the ionization reaction rate $\langle\sigma_i^p v_p\rangle$.

In figure 7.5 it is shown that the specific discharge current-voltage proportionality can be used to experimentally distinguish the space-charge and emission limited modes in the source. It also shows the significance of filament power. In the high power case the resistive filament heating power is approximately 16 % greater than the 555 W case, with a similar expected temperature difference. However, the electron emission scales strongly with temperature (see figure 3.2) and is expected to be several times greater. Therefore the high power case does not transition into the emission limited mode until a much greater discharge voltage is applied, compared to the other cases.

Secondary electron bombardment

- *Can secondary electron bombardment affect the ionization intensity?*

It is noted that the ionization reaction rate is not necessarily equal to the mean number of ionizations per primary electron and an enhancement of the actual ionization intensity may occur. If a primary electron with energy $\varepsilon_p \gg U_{ion}$, where U_{ion} is the neutral ionization potential, undergoes an ionizing collision the total excess energy $U_{exc} = \varepsilon_p - U_{ion}$ is partitioned between the scattered and ejected electron [42]. The electrons carrying this excess energy ε_{exc} can then potentially participate in another ionization process, provided that there is sufficient excess energy such that the ionization cross section is not insignificant ($\varepsilon_{exc} > U_{ion}$). The density of these electrons carrying significant excess energy is expected to be directly proportional to the primary electron density, where the energy originates from. Overall this effect is expected to cause an increased ionization intensity for high arc voltage scenarios. Quantification depends on the exact excess energy partitioning, which can be either equally split or favor the scattered electron depending on the particular incident energy. However, due to the bombardment energy of these electrons being minimally 24.5 eV less than ε_p in helium the ionization cross section will be approximately one order of magnitude smaller than that of the primary electrons. Hence the enhancement of ionization due to secondary bombardment is not expected to be significant.

7.2.2 Mode transition and space-charge limit

- *Can the mode transition and space-charge limited be identified?*

In chapter 4 it is described how the emission and space-charge limited modes behave, and in what way they affect operational performance. In section 4.1.2 equation 4.9 was derived from the principles of Child's law and double sheaths as an estimate of the space-charge limited current. Here an experimental characterization of the mode transition is presented. As described in section 5.3 the thermionic emission can be obtained during a shot. Figure 7.6 shows that when keeping all parameters fixed but increasing the filament power the discharge current saturates. The ion density profile also shows saturation, at $n_i \approx 1.4 \cdot 10^{17}$ m^{-3}. This saturation is a consequence of the transition from the emission limited mode into the space-charge limited mode, at which point no further increase in primary electron-caused ionization can occur. Increasing the thermionic emission further deepens the negative space-charge well, increasing the repulsion of primary electrons correspondingly.

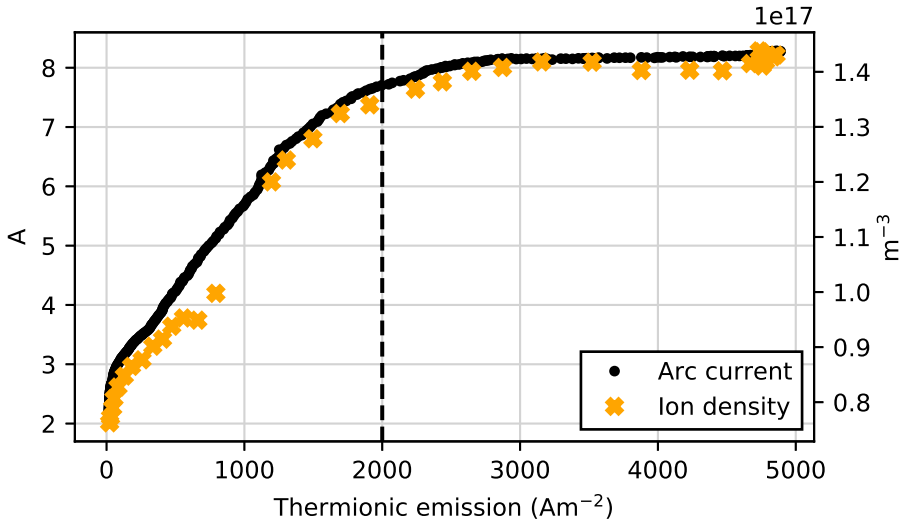

Figure 7.6: The transition of discharge current from emission-limited mode into space-charge limited mode. The transition occurs at approximately 2000 Am^{-2}, indicated by the dashed line. Prior to the transition the arc current increases linearly with thermionic emission, as is expected in the emission limited mode. The ion density profile shows a similar relation, indicating that ionization intensity is the underlying cause of the phenomenon.

The 'knee' of the transition from linear increase to saturation occurs at a primary electron emission of roughly 2000 Am^{-2}. This is lower than the space-charge limited current density that follows from equation 4.9, which is $19 \cdot 10^3$ Am^{-2}. However, as discussed in section 4.1.2, the predicted limit is a significant overestimate as the sheath thickness is assumed to be that of a high-voltage sheath, which does not take into account the presence of a double layer sheath. If Child's law, equation 4.8, is used to estimate the virtual cathode thickness for the experimentally found space-charge current of 2000 Am^{-2} a length of approximately ≈ 1 mm is found. This is equivalent to $27 \cdot \lambda_{De}$, or three times the high potential sheath thickness.

Another consideration is that the experimentally found limiting current density could be an underestimate due to the exponential scaling of the thermionic emission with temperature (equation 3.2). For the calculation of the thermionic emission an uniform temperature profile is assumed (the temperature obtained from the average resistivity). If a non-uniform temperature profile is assumed the total emission will be higher.

It is expected that the effect of space-charge is more prominent in helium than in the other background gases. As a consequence of the relatively high ionization potential unaccelerated electrons emitted from the filament do not significantly contribute to the ionization current in that region. However, if the the ionization potential is sufficiently low (and/or the background

gas pressure sufficiently high) there can exist an ionization region around the filament itself, neutralizing space-charge. Thus in the case of a high pressure, low ionization potential background gas the current is more likely to increase until becoming saturated at the thermionic current itself [27].

7.2.3 Ionization threshold

- *Does the arc current behave as expected in the region around the ionization threshold?*

An interesting area of the discharge current-voltage characteristics is the region around the ionization threshold. This can provide information on the device calibration and assumptions made in the theory study, particularly regarding primary electron monoenergeticity. If monoenergeticity is assumed, when performing a scan of low arc voltages prior to plasma ignition one expects a discharge current to appear as soon as the arc voltage becomes greater than the ionization potential, ie. $eV_{arc} \geq U_{ion}$. For helium $U_{ion} = 24.59$ eV. Such a current-voltage characteristic is shown in figure 7.7, where in order to amplify the low discharge currents the experiment is performed in relatively high pressure, compared to typical discharges.

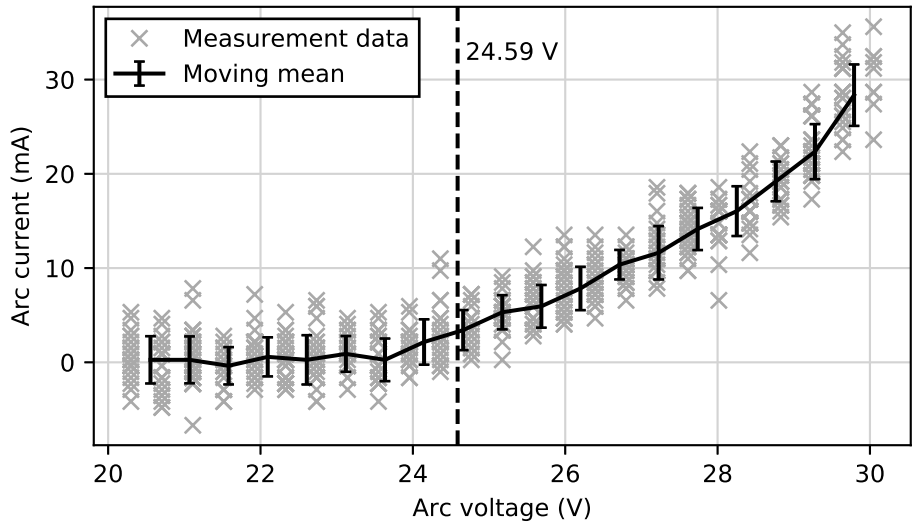

Figure 7.7: Arc current during a voltage scan around the ionization threshold. The vertical, dashed line indicates the threshold for helium from literature at 24.59 eV. High pressure amplifies the discharge current. The black line shows the moving mean with standard deviation. The moving mean departs from zero current between 23.6 and 24.1 V.

As can be seen in figure 7.7 the discharge current appears to depart from zero prior to the arc voltage reaching the ionization threshold, between 23.6 and 24.1 V. It was shown in equation 3.1 that the energy imparted on primary electrons in the potential fall is greater than the arc voltage. However, this cannot explain the lower apparent threshold; prior to any ionization there exists no plasma and thus the primary electrons do not fall through an additional plasma potential.

The threshold is at a fixed arc voltage only if monoenergeticity is assumed for the primary electrons. In reality some energy distribution exists, which has been experimentally detected in Electron Energy Distribution Function (EEDF) measurements in ion thrusters [24, 25]. Therefore the minimum arc voltage for ionization will be a function of the spread of this distribution, and can potentially be lower than U_{ion}. If this hypothesis holds the spread of the primary electron energy distribution would be approximately ± 0.8 eV, assuming a symmetric distribution. This is the discrepancy between the experimentally found minimum arc voltage and the helium ionization threshold energy from literature. This equates to a relative energy spread of ± 0.03 times the arc voltage.

7.3 Electron populations

7.3.1 Non-Maxwellian properties

- *What electron populations exist in the beam source plasma, and do their properties scale as expected?*

Electron populations determine the volumetric ionization intensity in the chamber and are therefore worth of investigation. Additionally, the presence of multiple populations has consequences for the interpretation of the Langmuir probe characteristic curves. In a relatively high density scenario electron-electron collisions dominate and the electrons thermalize into a Maxwellian energy distribution as described in section 3.2.2. This is the most probable energy distribution for a group of particles in thermal equilibrium. If the plasma density decreases this is no longer necessarily the case, and additional electron populations can coexist [39].

There are three distinct population that contribute to the electron energy distribution. The dominant population is that of thermalized electrons, which are defined by a relatively low Maxwellian temperature. The primary electrons are the most energetic contribution. They have an energy that is mainly characterized by the arc voltage (see equation 3.1). In section 7.2.3 it was discussed that these electrons likely have a relative energy distribution spread of approximately ± 0.03, and thus can be regarded as being close to monoenergetic. The third population arises in low pressure scenarios, where the electron mean free path is significant. In such a situation a fraction of electrons can fall through a part of the sheath and gain considerably more energy than the cold Maxwellian electrons. These are called '*hot*' electrons.

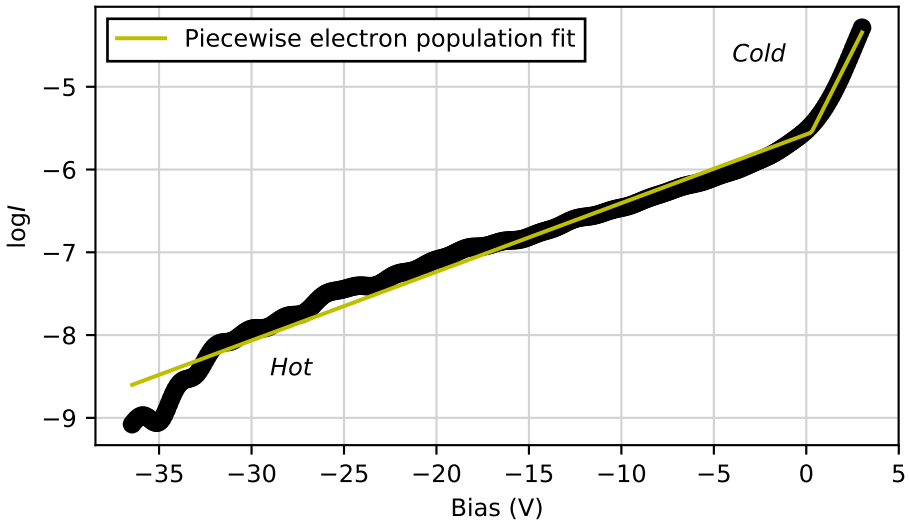

Figure 7.8: Langmuir probe observation of two distinct Maxwellian electron populations in the exponential growth region, indicated with *cold* and *hot*. The slopes are inversely proportional to electron temperature. From the vertical position of the transition the density ratio can be obtained.

The electron temperature is acquired from the Langmuir probe characteristic by means of an exponential fit in the electron growth region between the floating and plasma potential (see section 5.3.1. In certain experiments two well-defined slopes are observed, each corresponding to an electron population characterized by a certain temperature. This is shown in figure 7.8. The electron temperature is inversely proportional to the slope, as $\log I \propto \frac{eV}{T_e}$. It is hypothesized that the electrons collected in the regime with a strong negative probe bias correspond to the previously discussed hot population, and the larger, less energetic population ('*cold*') to the fully thermalized Maxwellian electrons. A piecewise fit is applied to obtain these temperatures. Using this method the highly energetic primary electrons cannot be detected, as their fraction is orders of magnitude smaller than that of hot electrons.

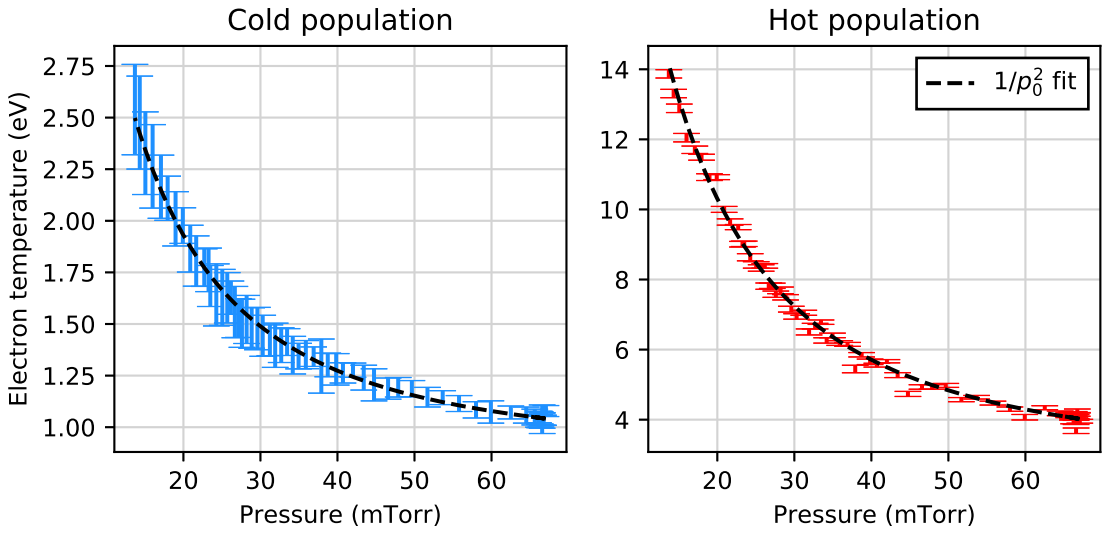

Figure 7.9: Temperature comparison of the electron species as function of pressure. Increasing the pressure decreases the temperature of both species. Error bars indicate the uncertainty in the Langmuir analysis. The curves are fit to the relation $T_e \propto 1/p_0^2$, which is expected during operation in arc current controlled mode.

The temperatures of the cold and hot populations can now be found as function of pressure, see figure 7.9. Similarly, the total fraction of hot electrons is obtained. This is shown in figure 7.10. The discharge current is equal to the total charged particle loss to the wall, which scales with species density and the square root of electron temperature. This was demonstrated in figure 7.3. It can be hypothesized that the density in a quasineutral plasma is linearly proportional to the background pressure. In the situation that the arc power supply is in the current controlled mode the discharge voltage will be regulated such that the discharge current I_{arc} is constant. From the constant $I_{arc} \propto n_i\sqrt{T_e}$ it then follows that $T_e \propto 1/p_0^2$, under the assumption that $n_i \propto p_0$. The temperature-pressure measurements of figure 7.9 are fit with such a relation. Mean relative residuals of $1.3 \cdot 10^{-2}$ and $2.3 \cdot 10^{-2}$ indicate proper convergence to the expected relation.

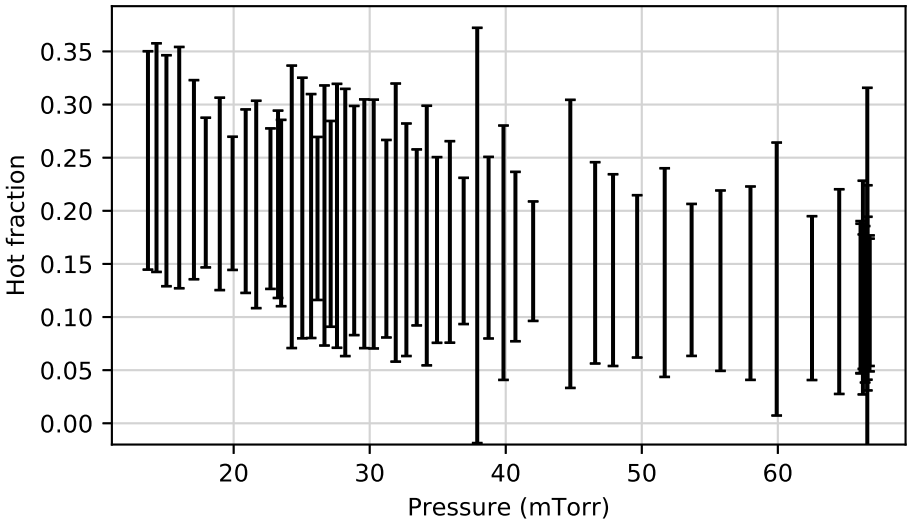

Figure 7.10: Total fraction of electrons belonging to the hot population, as function of pressure. The fraction decreases as the background pressure rises, but a significant uncertainty is present in the measurements.

The fractions shown in figure 7.10 contain a large relative error. Regardless, it can be concluded that these fractions are significant, with values of approximately 0.25 ± 0.10 in the lowest pressure region. This implies that the mean electron temperature, excluding primary electrons, is certainly higher than just that of the large cold Maxwellian population.

7.3.2 EEDF

- *Are non-Maxwellian properties found in the obtained EEDFs?*

The electron populations and presence of non-Maxwellian properties can be further analyzed by obtaining the Electron Energy Distribution Function (EEDF) from the Langmuir characteristics. This was an addition by Druyvesteyn [43] to the probe theory by Langmuir [35], discussed in section 5.3.2. The Druyvesteyn or Second Derivative method shows, under the assumption of an isotropic velocity distribution, the proportionality between the EEDF and the factor $\sqrt{V}\frac{\mathrm{d}^2 I}{\mathrm{d}V^2}$. Here $\frac{\mathrm{d}^2 I}{\mathrm{d}V^2}$ is the second derivative of the measured current-bias characteristic. Because the primary electrons are scattered by elastic collisions and reflected off surface fields isotropicity is assumed. From each voltage sweep of the Langmuir probe the EEDF can be obtained. It should be noted that the resulting EEDFs are strongly subjective to the chosen signal smoothing method, as a specific balance between noise reduction and loss of detail must be chosen. A scan of filter properties does show qualitatively similar EEDF profiles.

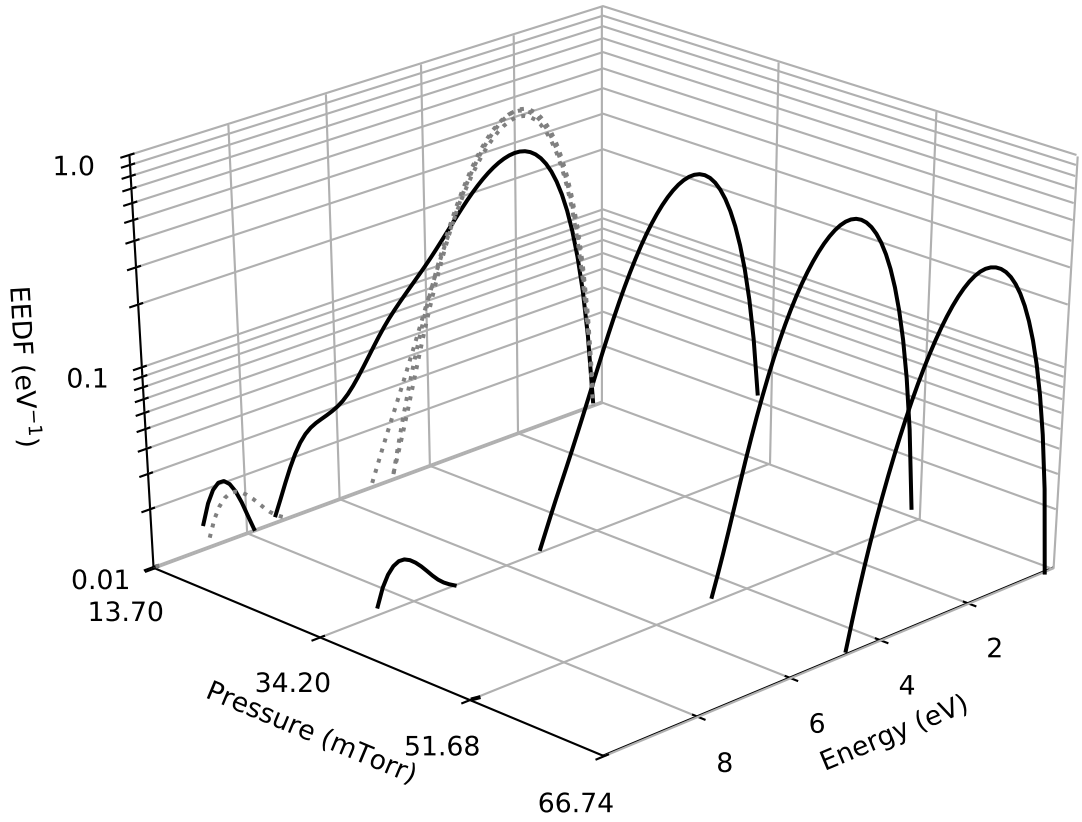

Figure 7.11: The Electron Energy Distribution Function (EEDF) for various pressures. A transition from a Maxwellian to a non-Maxwellian distribution is found. For comparison a projection of the EEDFs is shown on the far left plane (dotted lines).

In figure 7.11 the EEDFs demonstrate that for decreasing pressure the EEDF becomes increasingly non-Maxwellian. This is expected behaviour, and was also shown in the last section. From the hot electron fraction measurements of figure 7.10 it would be expected that the EEDF

at 34.20 mTorr also deviates. Besides the appearance of a detached peak at 8 eV however, it appears to be a fully Maxwellian profile similar to the higher pressure EEDFs. The total hot electron fraction is possibly in the lower bound of the uncertainty range for these pressures (0.05-0.10), and in the upper bound for the 13.70 mTorr profile (a fraction of 0.35).

A detached peak is observed in the low pressure EEDFs ($p_0 = 13.70, 34.20$ mTorr). This peak possibly corresponds to the hot population, albeit the temperature is lower than that found using the exponential slope fit method shown in figure 7.9. The peaks could also be an artifact from relatively small oscillations in the Butterworth filter response, which are amplified when taking the second derivative.

7.4 Spatial uniformity

- *What is the spatial structure of plasma parameters and potential distribution in light of the uniformity requirement?*

Using the linear motion capability of the custom-built Langmuir probe a spatial profile of various plasma parameters can be constructed. This can be used to evaluate the plasma uniformity, which is important in light of ion source criteria (see section 3.1, Requirement 2), and to evaluate the potential distribution as discussed in section 3.2.

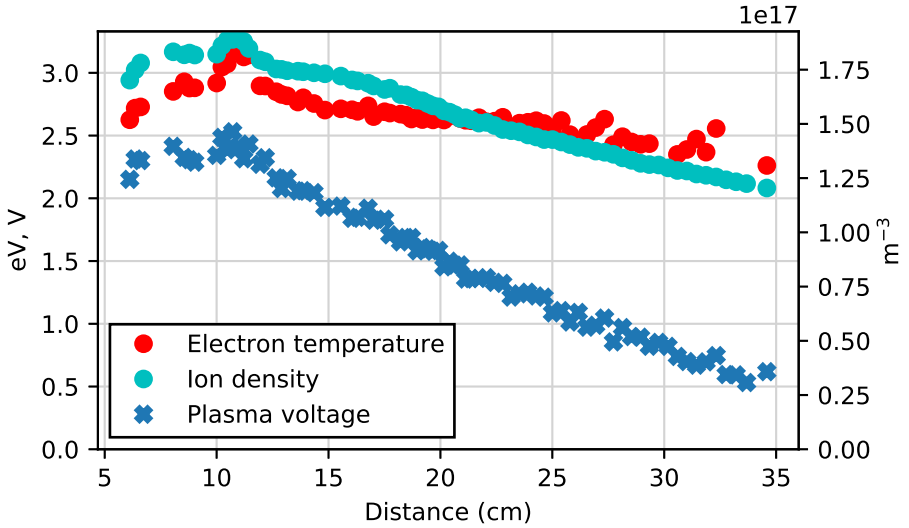

Figure 7.12: Probe translation during a shot showing the variation in electron temperature. The $x = 0$ position is the back plate and filament base. A peak is found at the location closest to the filament, with a decreasing profile as the probe is retracted.

In figure 7.12 the profiles along the central z-axis of the chamber are shown. The density drops along the measured distance due to the decreasing ionization intensity further from the filament location. The total obtained ion density fluctuation level is 57% max/min with a maximum of 1.9 and a minimum of $1.2 \cdot 10^{17}$ m^{-3}, which is greater than the maximum permissible fluctuation of 15% max/min as described by Requirement 2. However, it should be noted that density uniformity requirement described in section 3.1 concerns the fluctuation level of the plasma directly impingent on the accelerator grid, as opposed to along the entire central axis of the plasma. Measuring the spatial ion density profile near the exit plane could be the focus of a future study. The axial fluctuations near the exit plane along a distance of the order of the chamber radius is 10.5% max/min, which is within the criteria limits assuming that the radial profile has similar ion density gradients.

The plasma potential distribution as shown in figure 7.12 decreases linearly along the central axis. This corresponds to the theoretical profile shown in figure 3.1. The peak at $z = 10$ cm could be the result of poor Langmuir analysis at distances closer to the filament due to probe saturation. If the hypothetical result of section 7.2.2 holds the virtual cathode thickness equates

to approximately 1 mm, which is below the resolution of the spatial profile. Moreover, the close proximity to the high temperature filament would be destructive to the probe and might heat the tungsten probe tip to emissive levels, disturbing any potential measurement.

The plasma voltage measured is not raised by the arc voltage as shown in figure 3.1. The underlying reason is that, for safety purposes, the anode is grounded and the filament dropped to a negative potential instead as described in figure 5.4.

8. Insulation gasket investigation

- *What CLPS improvements can be suggested based on replication and failure mechanism analysis of the insulation breakdown during helium operation?*

The original goal and initial application of the new table-top beam source is the investigation of the issues surrounding helium operation in the DIII-D NBI systems, more particularly the formation of *arc spots* across the electrode gap. Mylar gaskets are located inside the gaps to provide electrical insulation. These arc spots, known in literature [44], arise as highly localized short-circuits between the cathode and anode, and damage the insulation gasket separating these plates (see the photographs in figure 2.3). They occur at non-regular intervals at seemingly random locations around the chamber circumference (as indicated in figure 2.5).

The phenomenon of arc spotting in the CLPS design was described as early as 1985 [7], during the initial commissioning. The sources were subject to 'frequent and severe' arc spotting. In development research conducted at the time it was found that plate materials with a higher melting temperature behaved more favorably in terms of the damage and frequency of arc spots located at the electrode gaps. Consequently several design modifications were made. These include covering the copper plates with a nickel layer, and the construction of a molybdenum shield structure mounted on the plates inside the chamber. This shield structure diminishes the plasma line-of-sight to the electrode gap. The modifications reduced the arc spotting severity to a level suitable for source operation in deuterium and hydrogen.

However, since this initial commissioning in the 80's no further modifications have been made, and prior to the design of the table-top source presented in this work no test stand for CLPS development existed in the United States. In this chapter the initial results of an investigation towards increased arc spotting during helium operation is discussed. The nature of these results is mostly *qualitative* as there are relatively large quantitative uncertainties and unknowns in many of the material properties, and the results of previous studies have been empirical.

8.1 Hypotheses

- *What are the failure mechanism hypotheses?*

The first step of the investigation involves analyzing the failure mechanism, or combination thereof. These mechanisms eventually lead to the formation of a self-sustained arc that bridges the gap between the cathode and anode plates. The main process of such a (non-thermal) arc is the thermionic emission from a relatively small, hot spot on the cathode. These are sometimes called 'microspots' in literature. Thermionic emission of electrons from the metal plate surface is sustained by and grows due to ionic bombardment heating. A certain threshold surface temperature initiates this self-sustained arc, which is characterized by the condition that the emission of electrons at that temperature is sufficiently high that the consequent ionization and ionic bombardment supply the cathode spot with the energy required to sustain the local temperature [44]. Several candidate hypotheses are defined:

1. **Plate heating**
   It can be hypothesized that ionic bombardment of the cathode plate heats (certain) areas of the metal surface to initiate sufficient thermionic emission to ignite an arc. The bombardment heating power to the surface corresponds that presented in section 4.1.1, see equation 4.2.

2. **Bombardment carbonization of gasket**
   Another hypothesis is that ionic bombardment leads to carbonization of the gasket material, destroying the insulating properties. A direct conductive path now exists from one

electrode to another. A current will run across this short-circuit, heating the electrode plates and initiating thermionic emission.

To elaborate further, the gasket material used is Mylar. Mylar, see table 8.1, is one of the trade names of the material BoPET, advertised as a strong and electrically insulating plastic. Because this material is a polymer it is subject to carbonization under energetic bombardment.

3. **Sputtered tungsten deposition**
   As was shown in section 4.2 the filament undergoes erosion and vaporization, especially during helium operation. This lost material can be deposited on internal surfaces, coating the gasket with a conductive layer. This conductive path can lead to failure, in a process similar to the one described in Hypothesis 2.

4. **Cathode self-sputtering**
   Both the plate heating and gas breakdown may be interpreted as a manifestation of (runaway) self-sputtering of the copper cathode. Helium - and potentially argon - sputters copper particles into the source. These sputtered copper particles have a short ionization mean free path and consequently have a certain probability to return and bombard the the cathode surface, creating a self-sustained self-sputtering effect [45]. The consequential release of metal particles with a low ionization potential can lead to the formation of a destructive metal vapor arc.

It should be noted that the timescales upon which these mechanisms act differ. Especially in the case of filament loss deposition the effect is cumulative, as was described in section 4.2, and an initial loss modelling study shows that the formation duration of a monolayer can be in the range of hours (helium operation) to tens of hours (hydrogen and deuterium operation). This is under the assumption that all sputtered and evaporated filament material is deposited on the walls, and that all internal surfaces are coated equally. The gasket carbonization is also a cumulative effect, but is expected to occur on shorter timescales.

8.2 Failure replication

- *Can the failure be replicated?*

Each of the main hypotheses involves a mechanism that becomes more severe with increased discharge voltage. This is either increased ionic bombardment energies, or increased sputtering.

By ramping the discharge voltage beyond 100 V it was attempted to reproduce the appearance of arc spots. This occurred at approximately 120 V. During the arc event the discharge current spiked to > 25 A simultaneously with a discharge voltage drop to a fraction of a volt. The initial observations were the destruction of gasket material in a number of spots located at the insulation-plasma interface. Examining the most severe spot (see the photographs of figure 8.1) it is found that a small section of the sandwich of the stainless steel back plate and the copper filament plate had been molten, indicating local temperatures in excess of 1700 K. The arc spotting damage is similar to that observed in CLPS insulation breakdown failures, as shown in figure 2.3.

It can be seen in the photographs of figure 8.1 that on the electrode plates oxidation layers formed, which are an effect of oxygen impurities in the background gas and of the temperature developed during the arc event. The number of oxidation layers indicate the heat intensity and can be used to qualitatively compare arc spots, and find the one through which the highest current was dissipated. They correspond to the contours of maximum temperature during the failure.

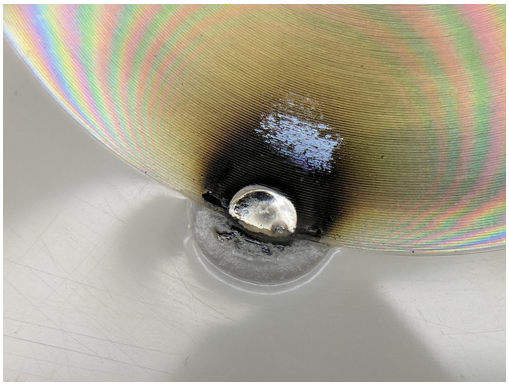

(a) Arc spot damage across the insulation gasket on the stainless steel back plate. The black residue is carbonized Mylar gasket. The Mylar is also molten and fused to the stainless steel flange.

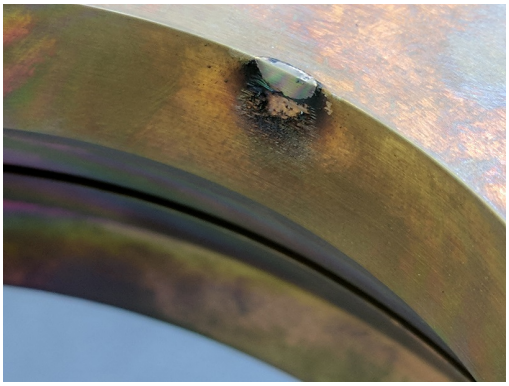

(b) Damage to the copper filament plate, corresponding to the arc spot damage shown in figure (a).

Figure 8.1: Replicated arcing damage during helium operation across the stainless-gasket-copper sandwich. On both plates craters of molten metal are discovered.

8.3 Experimental observations

- *What is experimentally observed?*

In this study several preliminary experiments were conducted with a number of design and operational changes, and more are planned in future research. During several dry runs, where the source is ran at high discharge voltage without the presence of a plasma, no arc spot formation is observed. As long as a tungsten coating or gasket carbonization is not already present, this is in accordance with the proposed hypotheses.

Several proposed alternative designs are shown in figure 8.2, of which a number were investigated in this study. These will be presented in this section.

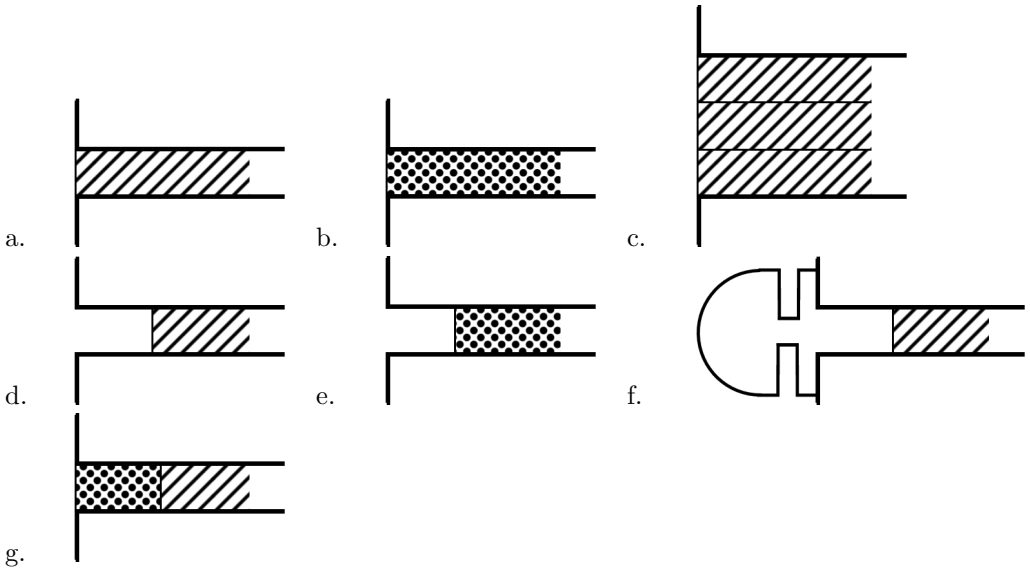

Figure 8.2: Various proposed insulation gasket designs. These can be described by a. Single Mylar gasket, b. Single Mica gasket, c. Triple Mylar gasket, d. Receded Mylar gasket (by 0.25 in $\approx$ 0.64 cm), e. Receded Mica gasket (by 0.25 in $\approx$ 0.64 cm), f. Macor gap shield, g. Combined Mylar/Mica design.

8.3.1 Recessed gasket

Some of the hypotheses presented in section 8.1 rely on the formation of a conducting path from one electrode to another, which is facilitated by the insulation itself. More specifically, in Hypotheses 2 and 3 the presence and plasma interaction of a physical piece of gasket material is critical to the failure mechanism. Thus, recessing the insulation and thereby reducing the exposure of the gasket material to the plasma would improve the reliability of the source. This corresponds to designs d. and e. as shown in figure 8.2. The designs are identical but the latter uses Mica as gasket material instead, see section 8.3.2.

The result of operation with a recessed gasket can be seen in figure 8.3. Observational analysis indicates that arcing damage occurred around the entire circumference of the chamber, and also inside the gap where insulation was removed. The worst damage was located near the plate edge. The underlying physical reason could be the stronger surface field near this sharp feature. In conclusion, the manifestation of the failure mechanism at work is non-reliant on the presence of a piece of insulation.

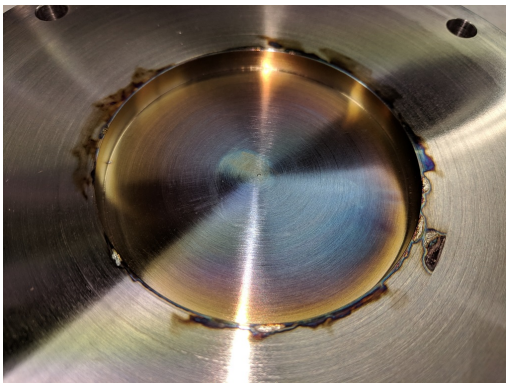

Figure 8.3: Arcing damage in receded gasket design.

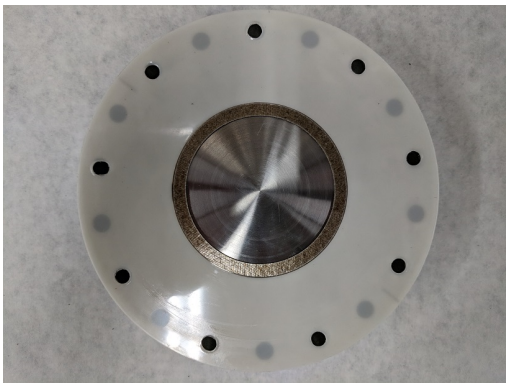

Figure 8.4: New gasket design with inner annular ring of Mica.

8.3.2 Alternative gasket material

As an alternative to Mylar the gasket material Mica was tested in the source. A comparison of properties can be seen in the table below. The underlying reasoning is that Mica is more temperature resistant and cannot carbonize, albeit having a lower (vacuum) dielectric strength.

Table 8.1: Estimates of insulation gasket material properties provided by the manufacturer DuPont Teijin Films. T_{max} is maximum operational temperature and E is dielectric strength.

Material	Structure	Thickness	T_{max}	E
Mylar (conventional)	Polymer	0.4 mm	420 K	79 kVmm^{-1}
High-temperature Mica	Resin-infused ceramic	0.3 mm	970 K	25 kVmm^{-1}

Several designs with this material were developed, see the dotted areas in figure 8.2. The gaskets are under significant compressional pressure to ensure the electrode gap is vacuum-tight. Because Mica is a ceramic and therefore prone to shattering, the initially tested design was g. In this design Mica is the plasma-facing material, and a regular sheet of Mylar is located behind it to provide compressional strength. A photograph of this design is shown in figure 8.4.

During source operation with design g it was found that arc spot formation was frequent and occurred at discharge voltages as low as 40 V. This indicates that Mica is unsuitable for electrode insulation purposes in low-temperature plasma environments.

8.3.3 Gasket stack

An increase in inter-plate distance can be achieved by the use of a thicker insulation gasket or the use of multiple stacked gaskets. The concern with a gasket stack is the compatibility with vacuum operation; grooves in the metal plates allow for the insertion of rubber o-rings that provide a vacuum seal, but those cannot be inserted between two gasket layers. During experiments it was found that a triple gasket stack, as shown in design c, does not perform as well as a single sheet vacuum-wise but is able to hold pressure at approximately 10^{-4} mTorr.

This design could not be tested extensively, but operation at arc voltages of 120 V did not result in issues after conditioning of the source (ie. gradually increasing the density and voltage).

8.4 Failure matrix and discussion

- *What conclusions can be deduced from a constructed failure matrix?*

A failure matrix is a matrix that compares hypotheses and observations, and can be used to infer conclusions on the mode of failure. Based on the hypothesized mechanisms presented in section 8.1 and the observations from section 8.3, the matrix shown in table 8.2 is constructed.

Table 8.2: Failure matrix of the gasket breakdown investigation. The matrix examines whether the hypotheses are valid in view of the experimental observations.

Observation →	More severe for helium atomic properties	More severe for higher arc voltage	More severe for higher pressure	Occurs without gasket presence	Improved with reduced plasma line-of-sight	Improved with increased gap width	Develops within single shot
1. **Plate heating**	no	yes	yes	yes	yes	yes	yes
2. **Bombardment carbonization**	yes	yes	yes	no	yes	no	no
3. **Sputter deposition**	yes	yes	yes	no	yes	no	no
4. **Cathode self-sputtering**	yes	yes	yes	yes	yes	yes	yes

The primary experimental observation relating to the motivation of this thesis is that the source reliability is diminished during helium operation, indicating that any applicable failure mechanism is more severe under at least one of the conditions involved with helium operation. These are the particular atomic properties of helium, such as ionization energy, operation at higher discharge voltages (ie. increased bombardment energies) and at higher background pressures (ie. increased ionic fluxes). All hypotheses discussed are in agreement with these conditions, however special consideration is required for the plate bombardment heating mechanism. The temperature threshold upon which thermionic emission becomes sufficient to sustain an arc is, in conjunction with others, a function of the amplification enhancement of electron current leaving the cathode. This amplification diminishes in helium due to the increased ionization potential.

Section 8.3.1 shows that arc spot breakdown takes place regardless of the presence of an insulating gasket, thus regardless of the interaction between an insulating surface and the plasma. From this can be deduced that Hypotheses 2 and 3 are not the primary failure mechanisms. Moreover, since these mechanisms accumulate on or affect the entire insulating surface simultaneously, they are not dependent on the gap width. It was found that, on the contrary, an

increased gap width seems to reduce the problem of arc spotting. This further decreases the likelihood of these hypotheses.

In literature am empirical equation is found which relates to the threshold current required for the formation of a metal vapor arc [44, p. 259]. This equation is given by $I_{min} = 2.5{\cdot}10^{-4} T_{boil}\sqrt{\lambda}$, in A, where T_{boil} is the boiling temperature of the metal in K and λ the heat conduction coefficient in $\mathrm{Wcm^{-1}K^{-1}}$. Evaluating this threshold current yields 0.17 A for a stainless steel electrode, 1.4 A for copper, and 1.9 A for tungsten. The discrepancy between copper and stainless steel corresponds to experiments, where it was found that the arc spotting between the steel-copper plates was more frequent and more damaging than between the copper-copper plates. Furthermore, this equation agrees with the empirical observation from [7] that electrode surface materials with higher melting temperature are more breakdown resistant, under the assumption that melting and boiling temperature are strongly correlated.

Taking into account all the above no firm conclusions can be made on the outcome of the study yet, but the metal vapor arc formation mechanism presented by Hypothesis 4 is strengthened by both past empirical observations and the present study. Indeed it makes sense that the breakdown itself is not facilitated by helium but by metal vapor, as the helium ionization potential is significantly higher than hydrogen or deuterium and thus a smaller breakdown probability would exist.

Based on this preliminary conclusion several design modifications that can mitigate the arc spot formation, or reduce it to manageable levels, can be presented. The primary method is an increase in gap width, which can readily be achieved through the use of thicker or stacked gaskets. Additionally, a molybdenum shield covering the gap and overlapping the electrode edges, as described in [7], could be developed and tested on the small source. Furthermore placement of permanent high temperature magnets in the electrode near the gap could be considered, which would create additional magnetic cusps in the gap vicinity and reduce or entirely prevent the ionic bombardment of the electrode gap that seems to be at the root of the issue. Lastly, an analysis of potential coating materials could result in other candidate materials, which could also be tested.

The team at the EAST tokamak in Hefei, China, has offered to make a full-scale CLPS source available for the further investigation of methods based on the findings presented in this thesis and in continuations of this work.

9. Conclusion and outlook

In this thesis the successful development, characterization and preliminary application results of a novel, table-top Neutral Beam ion source are presented. The need for such a device arose from the desire for the ability to test and demonstrate improvements for the Neutral Beam sources at DIII-D, particularly regarding helium operation.

To this end the most important concepts and criteria in beam source operation were identified and investigated. Particularly the need for primary electron confinement, uniform ion density, and low ion temperature were deemed important and were taken account in the design considerations regarding the development of the scaled-down source. Furthermore the capability of steady-state operation and diagnostical flexibility is considered important in light of performance and reliability testing. Steady-state operation is achieved through active cooling of the walls and diagnostical flexibility through a number of interchangeable ports that provide options for diagnostics. In parallel with the source development computational modelling was performed in order to verify the confinement properties. Qualitative analysis of the results suggest satisfactory confinement.

The plasma in the new source was experimentally characterized and compared to the expectations from theory and literature based on three aspects relevant to the task of the device. These aspects are arc current, which directly corresponds to beam performance, an analysis of the EEDF, which dictates the ionization intensity in the source, and spatial uniformity, one of the main beam source criteria.

It was shown in theory and experimentally demonstrated that two distinct modes exist and greatly affect the arc current, namely the emission limited and the space-charge limited modes. Temperature fluctuations of the filament due to ion bombardment and backstreaming electrons lead to unwanted instability of thermionic emission, resulting in the desire for the source to operate in the space-charge limited mode. In this mode a negative space-charge develops around the filament, which imposes a limit on the current of primary electrons entering the source plasma. An estimate for this emission limit is derived and found to agree with experimental results under the assumption of a virtual cathode thickness that is roughly three times that of a high potential sheath. Experimentally the relation between discharge current and arc voltage is further examined. It is shown that these parameters are directly correlated due to the combined effect of two mechanisms; an increase of arc voltage results in an increased space-charge permissible primary electron flux and a greater electron impact ionization cross-section. This is used to distinguish the two emission modes in discharges.

In low pressure scenarios a non-Maxwellian electron energy distribution is found. In addition to the primary electrons so-called hot and cold thermal populations are present. The bulk of electrons belong to the cold population, with a total fraction of the order of 10 to 20% belonging to the hot population. The hot population gains energy in the sheath potential drop, and it is shown that their mean free path in this region grows which decreasing pressure. Furthermore, it is hypothesized that during operation with a controlled discharge current the proportionality $T_e \propto 1/p_0^2$ holds. Experimental observation show agreement with this relation.

The spatial profile of plasma parameters was obtained, primarily in order to demonstrate ion density uniformity. It was found that the variability in the spatial ion density profile is greater than described as desirable by other authors. However, the density fluctuation measured is along the entire central axis of the plasma as opposed to the profile on the acceleration grid, which is most relevant to performance. Assuming the axial and radial ion density gradients are similar in this region a fluctuation level is found that falls within the criterion.

Using the new source a study was conducted on the issues related to helium operation in CLPS sources, particularly the phenomenon of arc spot development across the insulation gaskets between the electrodes. The failure was successfully replicated by an increase in discharge voltage. Several candidate hypotheses regarding the failure mechanism were defined and tested

through qualitative observations. To achieve this a number of experimental design changes were applied to the newly built source. The most important observation is that the mechanism is non-reliant on the physical presence of gasket material. Based on the constructed hypothesis-observation matrix one can infer that cathode self-sputtering is the most likely hypothesis. Several design modifications can be proposed based on this preliminary conclusion, however a continuation of this study is necessary. Building upon the findings presented here and in future continuations of this study development testing is proposed on a CLPS source at the Experimental Advanced Superconducting Tokamak (EAST) in Hefei, China, which is scheduled to take place in late 2018.

Outlook

Beyond the insulation investigation, it is proposed that future studies using the newly built source focus on the examination of alternative magnetic field configurations, such as a filter field or supercup field. These alternative configurations may lead to an overall increase in source efficiency through an improved species mixture and spatial uniformity near the accelerator grid, but may have poorer confinement properties than the multicusp design. Additionally, the miniature source would be suitable for the exploration of primary electron generation using hollow cathodes as opposed to heated filaments. This has major benefits, as the filaments lie at the origin of several reliability issues. Indeed, hollow cathode-driven sources for NBI have been described in literature and are in active development at Lockheed Martin Skunk Works.

The implementation of several additional diagnostics is suggested, primarily to improve measurements of parameters relevant to operation and performance, namely the EEDF, IED, and species densities. The EEDF measurement can be improved by implementation of the Boyd-Twiddy method. Measurement of the IED is currently absent but would contain valuable information regarding source performance. A RFEA probe could readily obtain this data. Furthermore, weak tungsten and electrode material densities could be obtained by the addition of a mass spectrometry, which is available at the DIII-D site. If an acceleration grid is added, which is planned as a future project, a calorimeter could be used to diagnose beam optics and power.

Concluding, for the first time since the commissioning of the NBI system in the 1980's research to suggest improvements on a variety of aspects of the CLPS source and therefore consequently significantly increase DIII-D research capability was performed on a table-top, steady-state beam ion source built specifically for this purpose.

Acknowledgments

This work was supported by the US Department of Energy under DE-FC02-04ER54698.

I would like to express my gratitude to my supervisors at General Atomics, Brendan Crowley and Tim Scoville, for their great support and the large amount of time they spent on the project during both discussions and hands-on work. I would also like to thank the rest of the Neutral Beam group at DIII-D, namely Joe Rauch, Russell Mueller, Ashley Harris, and Matt Madruga for their company and help in the lab, and also Carl Fremlin for his eagerness and work during the development process.

Furthermore I would like to thank Humberto Torreblanca for his motivational career insights and allowing me the honor to meet Francis F. Chen at UCLA.

On the Dutch side I would also like to thank my TU/e supervisors Roger Jaspers and Ana Sobota for bringing me in contact and having many helpful discussions and suggestions. Of course thanks and greetings also go out to my fellow students and members of the TU/e Fusion Group, without whom I would not have been so inspired to take on this challenge.

Finally I would like to sincerely thank FuseNet, the European Fusion Education Network, for providing financial support.

Thanks,
Jasper

References

1. J. L. Luxon, *Nucl. Fusion* **42**, 614 (May 2002).
2. H. Chundong, *Plasma Sci. Technol.* **14**, 567 (June 2012).
3. J. H. Kamperschroer *et al.*, presented at the 17th IEEE Symposium on Fusion Engineering (Oct. 1997).
4. B. Crowley, J. Rauch, J. T. Scoville, S. K. Sharma, B. Choksi, presented at the 26th IEEE Symposium on Fusion Engineering (June 2015).
5. J. D. Lawson, *Proc. Phys. Soc. B* **70**, 6–10 (Jan. 1957).
6. M. C. Vella *et al.*, *Rev. Sci. Instrum.* **59**, 2357–2365 (Nov. 1988).
7. M. C. Vella, *et al.*, presented at the 11th Symposium on Fusion Engineering (Nov. 1985).
8. K. W. Ehlers, K. N. Leung, *Rev. Sci. Instrum.* **50**, 1353–1361 (Nov. 1979).
9. Y. Xie *et al.*, *J Fusion Energ* **33**, 275–278 (Jan. 2014).
10. R. M. Hong *et al.*, presented at the 21st IEEE Symposium on Fusion Engineering (Sept. 2005).
11. A. W. Chao, M. Tigner, *Handbook of Accelerator Physics and Engineering* (World Scientific Publishing, 1999).
12. D. J. Campbell, presented at the 24th IAEA Fusion Energy Conference (Oct. 2012).
13. J. T. Scoville, "Ion source damage due to helium beam operation" (General Atomics, San Diego, US, Feb. 2017).
14. W. B. Kunkel, *Rev. Sci. Instrum.* **61**, 354–359 (Jan. 1990).
15. F. Ebersohn, R. Sullivan, presented at the 59th Meeting of the APS Division of Plasma Physics (Oct. 2017).
16. D. M. Goebel, I. Katz, *Fundamentals of Electric Propulsion* (Wiley, 2008).
17. C. R. Crowell, *Solid-State Electron.* **8**, 395–399 (Apr. 1965).
18. M. Kiziroglou, X. Li, A. Zhukov, P. de Groot, C. de Groot, *Solid-State Electron.* **52**, 1032–1038 (July 2008).
19. Y.-K. Kim, M. E. Rudd, *Phys. Rev. A* **50**, 3954–3967 (Nov. 1994).
20. D. M. Goebel, R. E. Wirz, I. Katz, *J. Propul. Power* **23**, 1055–1067 (Oct. 2007).
21. J. D. Huba, *NRL Plasma Formulary* (Naval Research Laboratory, 2013).
22. R. Moore, presented at the 7th Electric Propulsion Conference (Mar. 1969).
23. D. Bohm, *The Characteristic of Electric Discharges in Magnetic Fields* (McGraw-Hill, New York, 1949).
24. Y. Hayakawa, K. Miyazaki, S. Kitamura, presented at the 25th AIAA Joint Propulsion Conference (July 1989).
25. D. Herman, A. Gallimore, presented at the 41st AIAA Joint Propulsion Conference (July 2005).
26. T. Durakiewicz, S. Halas, *Int. J. Mass Spectrom.* **177**, 155–161 (Sept. 1998).
27. I. Langmuir, *Phys. Rev.* **33**, 954–989 (June 1929).
28. C. D. Child, *Phys. Rev. I* **32**, 492 (Jan. 1911).
29. I. Langmuir, *Phys. Rev.* **2**, 450 (Dec. 1913).
30. J. G. Andrews, J. E. Allen, *Proc. Royal Soc. A* **320**, 459–472 (Jan. 1971).

31. R. Hong *et al.*, presented at the 13th IEEE Symposium on Fusion Engineering (Oct. 1989).
32. Y. Yamamura, H. Tawara, *At. Data Nucl. Data Tables* **62**, 149–253 (Mar. 1996).
33. H. A. Jones, G. M. J. Mackay, *et al.*, *Phys. Rev.* **30**, 201 (Aug. 1927).
34. P. D. Desai, T. K. Chu, H. M. James, C. Y. Ho, *J. Phys. Chem. Ref. Data* **13**, 1069–1096 (Oct. 1984).
35. I. Langmuir, *Science* **58**, 290–291 (Oct. 1923).
36. S. Butterworth, *Experimental Wireless* **7**, 536–541 (Oct. 1930).
37. H. M. Mott-Smith, I. Langmuir, *Phys. Rev.* **28**, 727–763 (Oct. 1926).
38. F. F. Chen, J. D. Evans, W. Zawalski, *Plasma Sources Sci. Technol.* **21**, 055002 (Aug. 2012).
39. B. Crowley, S. Dietrich, *Plasma Sources Sci. Technol.* **18**, 014010 (Nov. 2009).
40. *COMSOL MultiPhysics™*, version 5.3, Apr. 2017.
41. A. Savitzky, M. J. Golay, *Anal. Chem.* **36**, 1627–1639 (July 1964).
42. K. R. Asmis, M. Allan, *J. Phys. B: At. Mol. Opt. Phys.* **30**, 167–173 (Mar. 1997).
43. M. J. Druyvesteyn, *Z. Physik* **64**, 781–798 (Sept. 1930).
44. Y. P. Raizer, *Gas Discharge Physics* (Springer-Verlag, 1991).
45. A. Anders, S. Anders, M. A. Gundersen, A. M. Martsinovskii, *IEEE Trans. Plasma Sci.* **23**, 275–282 (June 1995).
46. *Python*, version 3.6, Dec. 2016.
47. *NumPy*, version 1.13.3, Sept. 2017.
48. *SciPy*, version 0.19.1, June 2017.
49. *PlasmaPy*, version prerelease, Dec. 2017.

A. Additional photos

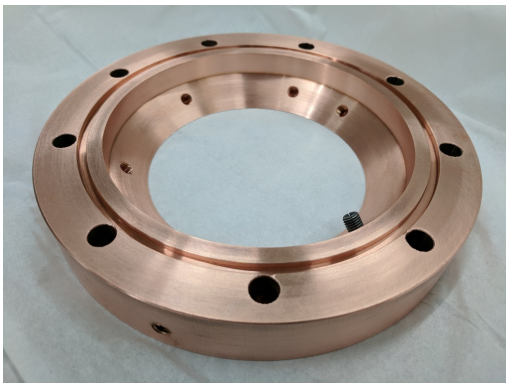

(a) 'Negative' filament plate.

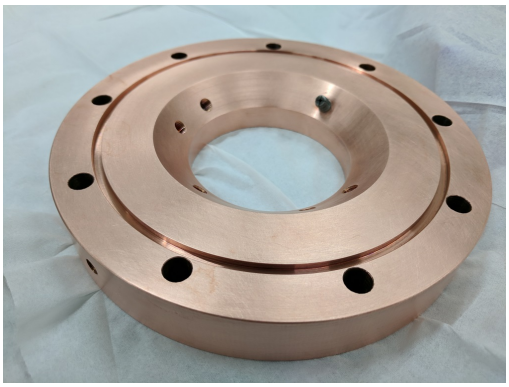

(b) 'Positive' filament plate.

Figure A.1: Photographs of the copper filament flanges. The plates are attached to the chamber with insulated bolts through the bolt holes around the perimeter. The inner holes are attachment points for up to 4 filaments. The choice of electrical polarity is arbitrary.

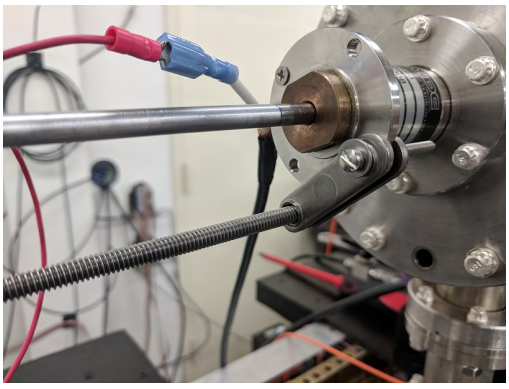

(a) Threaded rod attached to the chamber parallel to the Langmuir probe tube.

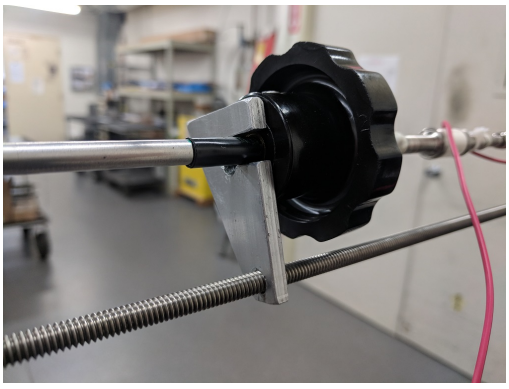

(b) Fixed piece connecting the threaded rod and Langmuir probe handle.

Figure A.2: Photographs of the threaded rod allowing constant linear probe motion.

B. Software

A software codebase was written for the experiment. It is composed of three parts: experiment control, data acquisition and data analysis. These will be discussed briefly. The entire codebase is written in Python 3.6 [46]. Python is chosen because it is an open source and general purpose programming language, and many available scientific modules can be leveraged. These include *NumPy* [47] (scientific computing), *SciPy* [48] (data analysis and fitting), and *PlasmaPy* [49] (plasma physics). Furthermore, several devices are accompanied by a dedicated Python module.

B.1 Control

The task of the control system is to provide functions to send and receive signals from the devices, and to communicate with the experiment operator. The aim is also to provide a completely digital interface with the experiment, so that remote operation is possible and no (expert) local supervision necessary.

On top of the control functions a Graphical User Interface (GUI) was built, hence no codebase familiarity is required to operate the setup. The GUI consists of three windows: a console window that shows raw information, a window with live data views (written with *pyqtgraph*), and a control window (written with *tkinter*). The control window provides buttons to digitally initiate and abort a discharge, set the overcurrent threshold (see section B.1.1), and operate the gas flow.

Discharge definition

A discharge is defined programmatically by a sequence of interactions with the experiment separated by set amounts of time. This sequence can then be initiated and aborted with the user interface. The available commands in the discharge definition are:

- Adjusting the desired arc voltage **or** current setpoint.
- Adjusting the desired filament current setpoint.
- Adjusting the desired background pressure.

These command variables can either be a fixed value or a function of time. Additionally, the discharge definition dictates when to initiate and stop the data acquisition for each shot.

B.1.1 Overcurrent protection

Internal shorts are expected (see section 2.2.3) and can potentially cause significant damage if not dealt with properly. An overcurrent fault protection system is digitally implemented with a response time of several milliseconds. If an arc current greater than the chosen overcurrent is registered the arc voltage is set to zero instantaneously. The arc voltage itself cannot drop to zero instantly but diminishes over time. This is due to the stored energy in the system and power supply.

B.2 Data acquisition

The task of the data acquisition system is to fetch and store data from the sensors, probe, and spectrometers. Sensor and probe signals are fed into a National Instruments USB-6008 and a LabJack T-7 Pro, respectively. The use of different acquisition devices allows simultaneous high precision sensor readings and rapid probe readings. The data from the Langmuir probe is

stored without processing, so that different techniques may be applied. Data from the Ocean Optics spectrometers is read and stored directly using the *SeaBreeze* module supplied by the manufacturer. This module also supports changing the integration time and other spectrometer settings.

B.3 Analysis

A separate module for data analysis was developed. This module is capable of reading any dataset from any shot number, and provides plotting functions for this data. Additionally the analysis module contains the Langmuir probe analysis as described in 5.3.2, and peak fitting functionality for the spectroscopic measurements.

PlasmaPy

Work was done to aid in the development of *PlasmaPy* [49]. This is an open source, community developed Python package specifically built for plasma physics. The Langmuir analysis presented in this thesis is to be implemented in *PlasmaPy*.